1995ApJ...441..182K

THE ASTROPHYSICAL JOURNAL, 441:182–199, 1995 March 1
© 1995. The American Astronomical Society. All rights reserved. Printed in U.S.A.

ROSAT PSPC OBSERVATIONS OF THE EARLY-TYPE GALAXIES NGC 507 AND NGC 499: CENTRAL COOLING AND MASS DETERMINATION

DONG-WOO KIM[1]
Harvard-Smithsonian Center for Astrophysics and Chungman National University, South Korea

AND

G. FABBIANO
Harvard-Smithsonian Center for Astrophysics, 60 Garden Street, Cambridge, MA 02138
Received 1994 July 8; accepted 1994 September 12

ABSTRACT

We present the results of a deep observation of NGC 507 and NGC 499 with the *ROSAT* PSPC. The X-ray emission of NGC 507 is extended at least out to 1000″ (458 kpc at a distance of 94.5 Mpc). The radial profile of X-ray surface brightness goes as $\Sigma_X \sim r^{-1.8}$ outside the core region. The radial profile is a function of energy such that the softer X-rays have a smaller core radius and a flatter slope. Spectral analysis reveals that the emission temperature, with an average of 1 keV, peaks at an intermediate radius of 2–3′ and falls toward the center (possibly decreases outward as well). The absorption column density is consistent with the Galactic line-of-sight value. The X-ray emission of NGC 499 is extended to 300″ and suggests a similarly cooler core. The cooler cores of NGC 507 and NGC 499 are strong evidence of the presence of cooling flows in these galaxies. Assuming hydrostatic equilibrium outside the cooling radius, the estimated mass-to-light ratio of NGC 507 is 97 ± 16 within 458 kpc, indicative of the presence of a heavy halo. Similarly, the mass-to-light ratio of NGC 499 is 89 ± 14 within 137 kpc. Near the edge of the X-ray–emitting region of NGC 507 we detect 19 soft, unresolved sources. These sources do not have optical counterparts and are significantly in excess of the expected number of background serendipitous sources. We speculate that they may represent cooling clumps in the halo of NGC 507. If there are many undetected cooling clumps distributed at large radii, then the radial profile of the X-ray surface brightness does not directly reflect the potential, adding uncertainty to the measurement of the binding mass; the gas mass could also be overestimated.

Subject headings: cooling flows — galaxies: individual (NGC 499, NGC 507) — X-rays: galaxies

1. INTRODUCTION

Soon after the *Einstein Observatory*'s discovery of X-ray-emitting hot gas in early-type galaxies, a debate ensued on the physical status of these halos and on using them as a tool for measuring the mass of the galaxies (for a review, see Fabbiano 1989). Initially, cooling flows were invoked to explain X-ray observations of early-type galaxies (for example, Fabian, Nulsen, & Canizares 1984; Sarazin & White 1987). These models reproduce observed global properties such as X-ray luminosity and emission-averaged temperature. However, until recently there has not been any direct evidence of the presence of cooling, with the exception of a few clusters of galaxies like Virgo and Perseus (e.g., Canizares, Market, & Donahue 1988), where X-ray spectroscopic observations revealed emission lines originating from the cooling gas. If cooling flows really take place in X-ray–bright early-type galaxies, the gas temperature should decrease within the cooling radius as the gas is falling toward the center. An important consequence of the presence of gaseous halos is the ability to measure the galaxy mass if these halos are in hydrostatic equilibrium. In many X-ray–emitting galaxies, these mass estimates suggested the existence of a large amount of dark matter. However, the uncertainties on the radial behavior of emission temperature and surface brightness, intrinsic to *Einstein* data, resulted in large uncertainties (Trinchieri, Fabbiano, & Canizares 1986). In particular, if the radial behavior of the temperature is not known, the presence of high external pressure could lead to the erroneous conclusion of the presence of large heavy halos (Vedder, Trester, & Canizares 1988; Bertin, Pignatelli, & Saglia 1993). External pressures are typically not considered in the derivation of these masses.

Accurate measurements of emission temperature and surface brightness distribution are necessary to confirm the existence of cooling flows in these galaxies and study their properties, and to measure their binding mass. To obtain these measurements, we have acquired deep *ROSAT* PSPC observations of NGC 507 and report the spatial/spectral behavior of its X-ray properties in this paper.

NGC 507 is the brightest member of a group of galaxies belonging to a poor cluster, the Pisces Cluster, which contains several subgroups (e.g., the NGC 383 group and the NGC 507 group). This cluster in turn belongs to the long, narrow main ridge of the Pisces-Perseus supercluster (see Wegner, Haynes, & Giovanelli 1993 for a large-scale distribution of galaxies in this region). Within its optical radius, NGC 507 (also Arp 229 and VV 207) has a close companion elliptical galaxy with a similar redshift, NGC 508 which is 90″ north of NGC 507, and there may be interaction between the two galaxies (Arp 1966). NGC 507 has a weak radio core (Parma et al. 1986) and it may have a dust lane in the center (Ebneter, Djorgovsky, & Davis 1988).

NGC 507 is one of the most luminous, extended X-ray sources among early-type galaxies (Fabbiano, Kim, & Trinchieri 1992) and its X-ray luminosity ($\sim 10^{43}$ ergs s^{-1}) is comparable to those of poor clusters (Kriss, Cioffi, & Canizares

[1] Mailing addresses: Chungnam National University, Taejon 305-764, South Korea and Harvard-Smithsonian Center for Astrophysics, 60 Garden Street, Cambridge, MA 02138.

© American Astronomical Society • Provided by the NASA Astrophysics Data System

1995ApJ...441..182K

1983). The *ROSAT* PSPC observation was motivated by the suggestion, based on the *Einstein* IPC data, that NGC 507 may have relatively a cool, absorbed core of X-ray emission (Kim & Fabbiano 1992; see Fabbiano 1993). We indeed find the signature of cooling in this galaxy core with the *ROSAT* PSPC, but do not confirm the excess absorption. The *Einstein* IPC image (Fabbiano et al. 1992) shows that while NGC 507 is the dominant X-ray source, another relatively strong source is associated with the elliptical galaxy NGC 499. We describe observational results for spatial and spectral analyses of both galaxies in § 2, and we compare these results with the *Einstein* data in § 3. We estimate the deprojected density and gravitational mass and discuss the implications of the observational results in § 4. Finally, we summarize our results in § 5.

2. OBSERVATIONS AND DATA ANALYSIS

The NGC 507 and NGC 499 field was observed by the *ROSAT* PSPC at two separate times, 1992 August 9–10 and 1993 January 8–9. The net exposure time is about 20,500 s (5600 and 14,900 s each). The observational parameters and basic physical parameters of the galaxies are listed in Table 1. The *raw* PSPC image of NGC 507/499 (the second, longer observation) is shown in Figure 1. Although no correction was applied, it is clear that extended diffuse emission is present inside the 20′ circle of the detector supporting structure. In addition, several pointlike sources are visible within the field of view.

Because of pointing uncertainty, the X-ray centroids of the two observations are not at the same sky coordinates once the data are aspect-corrected. For this reason, we have analyzed the two observations separately to determine radial profiles and spectral distribution for each. We then combined the counts in each radial bin relative to the centroid of the emission from the two observations to generate a radial profile. Similarly, the spectral counts from each channel were added to generate the total spectral distribution. We used the IRAF/XRAY package (developed at SAO) for the data analysis. We also used the program XSPEC (provided by the NASA–HEASARC) for the spectral analysis.

TABLE 1

BASIC PARAMETERS

Parameter	NGC 507	NGC 499
R.A. (J2000)[a]	1 23 40.1	1 23 11.6
Decl. (J2000)[a]	33 15 22	33 27 36
B_T^0 (mag)[a]	12.19	12.79
D (Mpc)[b]	94.5	94.5
D_{25} (arcsec)[a]	185	97
N_H (cm^{-2})[c]	5.3×10^{20}	5.3×10^{20}
PSPC observed date[d]	1992 Aug 9–10	1992 Aug 9–10
PSPC on time (s)[d]	5728	5728
PSPC Exp time (s)[d]	5600	5410
PSPC observed date[f]	1993 Jan 8–9	1993 Jan 8–9
PSPC on time (s)[f]	15290	15290
PSPC Exp time (s)[e,f]	14900	13920
σ_* km s^{-1} [g]	366	...
σ_{group} km s^{-1} [h]	595	...
log F_x (IPC) ergs s^{-1} cm^{-2} [i]	9.4×10^{-12}	3.0×10^{-12}

[a] Right ascension (R.A.), declination (Decl.), total face-on B magnitude (B_T^0), and major isophotal diameter measured at $B = 25$ mag arcsec^{-2}(D_{25}) taken from de Vaucouleurs et al. 1991 (RC3).

[b] Distance estimated by using $H = 50$ km s^{-1} Mpc^{-1} and an average group velocity of 4725 km s^{-1} (Wegner et al. 1993).

[c] Galactic line-of-sight H column density from Stark et al. 1992.

[d] Sequence number rp600254.

[e] Average exposure time within 3′ circle.

[f] Sequence number rp60025401.

[g] Stellar velocity dispersion from Faber et al. 1989.

[h] Group velocity dispersion from Wegner et al. 1993.

[i] IPC flux from Fabbiano et al. 1992. Fluxes were estimated in a energy range of 0.2–4.0 keV and $kT = 1$ keV was assumed. The count extraction radii are $r = 630''$ and $r = 210''$ for NGC 507 and NGC 499, respectively.

2.1. *Background Subtraction*

The standard *ROSAT* PSPC analysis software (SASS) provides background estimates for each observation. However, this background map does not represent the real field background when a very extended source is present as in this observation (see also Trinchieri et al. 1994). In Figure 2*a*, we compare the radial distribution of the background map with that of the exposure map, also generated by SASS. The latter contains the effect of telescope vignetting and shadowing by the window-supporting structures. The exposure map can be considered as a flat field for a given observation. It is clear that in the center of the field the background map contains excess emission over that expected from a uniformly extended background. This is also demonstrated by Figure 2*b*, where we show the observed data (source + background profile) divided by the exposure map (*solid line*), compared with a similarly treated background map (*dashed line*). Both unsubtracted data profile and background map profile flatten out at radius $r > 30'$ from the field center. However, the SASS background profile is not flat throughout the field, but increases between $\sim 5'$ and 30′. This demonstrates the inclusion of residual source emission in the background map. We adopt the dashed line (i.e., the flat surface brightness) as our background level. This corresponds to a background level determined locally at $r = 30'$–$40'$ from the field center where the count rate per unit area becomes flat. The background subtracted data are shown as points with error bars in Figure 2*b*.

A detailed discussion of the different PSPC background components can be found in Snowden et al. (1994). In summary, this background consists of a particle component (which is not vignetted) and X-ray component (auroral, scattered solar X-ray, cosmic X-ray, etc.), which is vignetted. In our background subtraction analysis, we have implicitly assumed that the field background is vignetted (see above). This is not a bad assumption in our case, since we estimate that the particle-contribution is $\sim 1\%$ of the total background (estimated from the master veto rate, see Plucinsky et al. 1993). Moreover, we have checked the time variation of our data to exclude short-term enhancements and scattered solar X-rays in the background. These, however, would be vignetted, so our analysis would subtract them correctly. Another background term, mentioned by Snowden et al. (1994) is afterpulse background. The afterpulse is present in PI channels near 11 after cosmic-ray hits. We do not use these low-energy channels in our analysis (see below).

To estimate the uncertainties of our background determination, and how it would affect the derived surface brightness profile of NGC 507, we used background maps generated from other observations which do not contain extended sources. As done in Trinchieri et al. (1994), we used four representative PSPC pointing observations: rp600009, rp600008, rp600017. and rp600520. In all of these observations, the second PSPC (PSPC-B) was used and the gain was at a low state. The radial profiles of the four background maps (PI = 7-240) produced by the standard SASS processing are very similar to each other and also similar to that of the NGC 507 exposure map (see Fig.

© American Astronomical Society • Provided by the NASA Astrophysics Data System

1995ApJ...441..182K

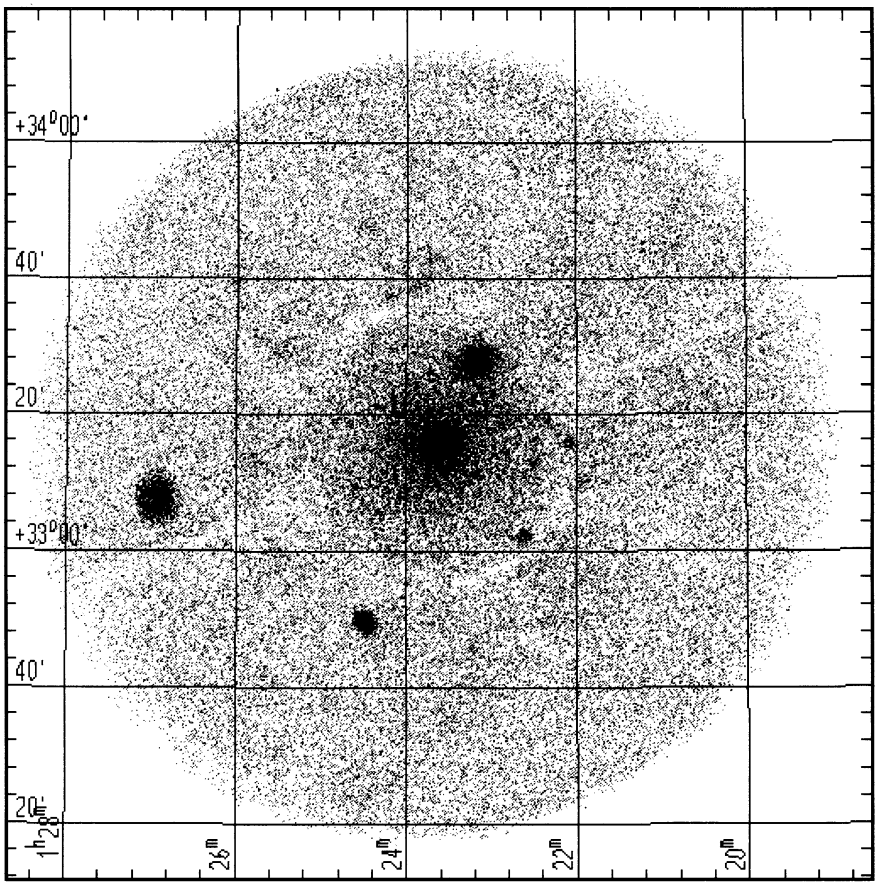

FIG. 1.—The raw PSPC image of NGC 507/499 field. No correction was applied.

3). Only one observation (rp600520) results in systematically lower counts in the central region (about 10%). Using different observed background templates, we find that the net source radial surface distribution does not change appreciably, When these differences are translated in errors in the parameterization of the surface brightness profile (see § 2.4), we obtain estimates of a core radius and slope all within 1% of each other, except the case of rp600250 which produces a ~3% flatter slope. All these values are well within the error bars of our estimates.

2.2. *Surface Brightness Distribution–Contour Map*

The X-ray contour map of the NGC 507 region is shown in Figure 4. The broadband image (0.1–2.4 keV), after exposure-correction and background-subtraction, is binned in 15″ bins, and smoothed with a Gaussian of $\sigma = 30''$. The contours are

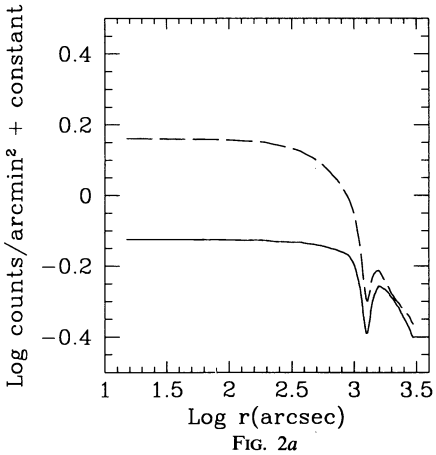

FIG. 2a

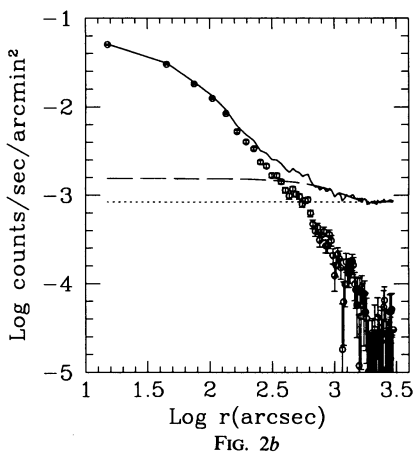

FIG. 2b

FIG. 2.—Comparison of background map and exposure map. (*a*) The radial profile of the background map (*dashed line*) and that of the exposure map (*solid line*) are plotted in unit of counts per unit area, but the normalization is arbitrary to easily compare two profiles. (*b*) The rate as a function of radius is made by dividing the image by the exposure map. The solid line is the source rate, the dashed line is the rate taken from the background map, the dotted line is the adopted background rate, and circles with error bars are the net rate.

© American Astronomical Society • Provided by the NASA Astrophysics Data System

1995ApJ...441..182K

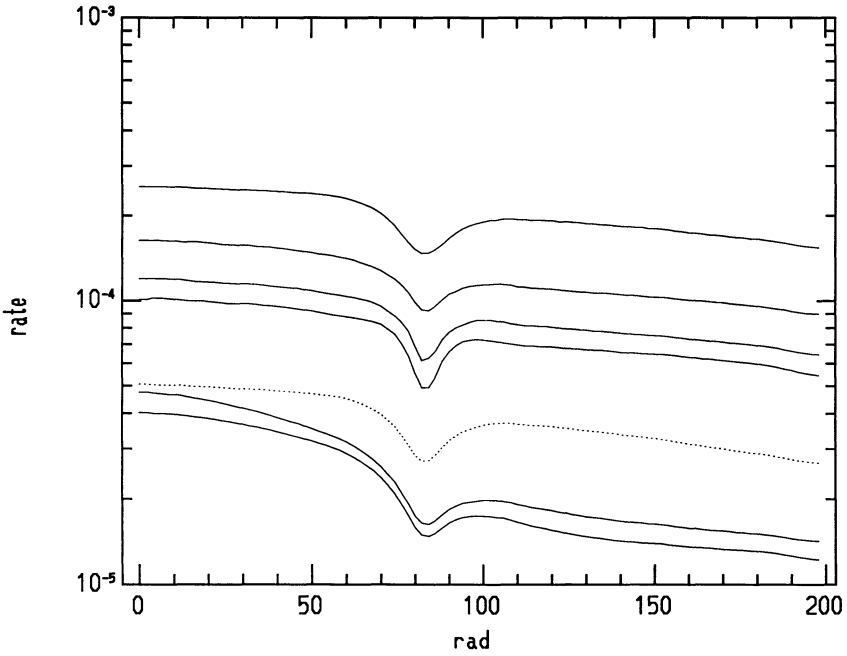

FIG. 3.—Comparison of background maps obtained from other PSPC observations. From the top, they are rp600009, rp600008, rp600017, and rp600520. The dotted line is the radial profile of the exposure map of this observation (rp60025401). The bottom two lines are radial profiles of the background maps of this observations (rp600245 and rp60025401). Normalizations are arbitrary.

plotted in units of counts arcmin^{-2} ks^{-1}. The lowest plotted contour is roughly at the 2 σ level, corresponding to 0.4 counts arcmin^{-2} ks^{-1}; other contours follow at 0.5 mag interval (i.e., a factor of 1.585). The figure shows two strong X-ray sources: the stronger is at the center of the field, corresponding to the optical position of NGC 507; the second strong source coincides with NGC 499 at 13.6 to northwest of NGC 507. Both sources were also detected with the *Einstein* IPC (Fabbiano et al. 1992). Four more prominent point sources are present in the *ROSAT* PSPC field: one at 7′ to the southwest of NGC 507, one at 18′ to the southwest of the NGC 507, and the other two outside the central 20′ circle (see Fig. 1). Also noticeable are many less intense peaks of emission near the edge of the X-ray–emitting halo of NGC 507. While the X-ray image of NGC 507

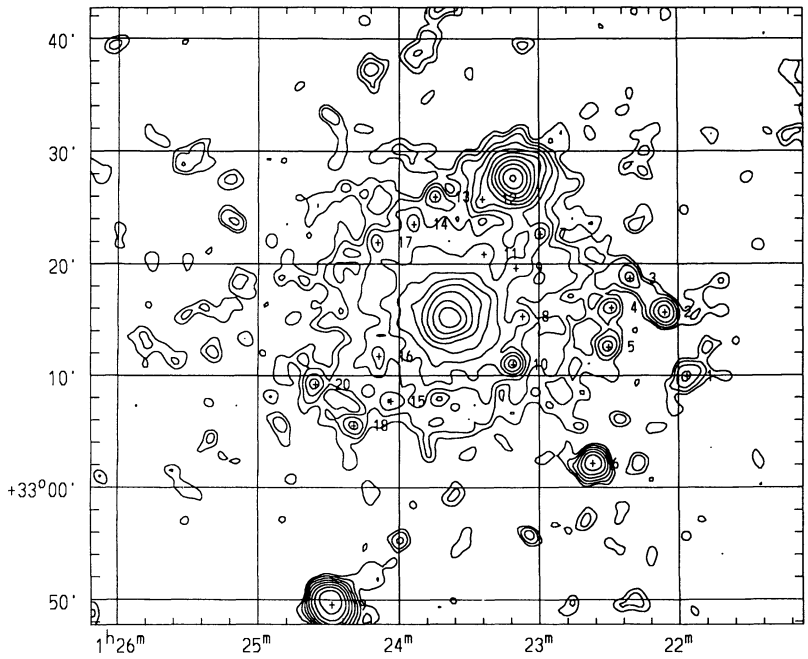

FIG. 4.—Contour plot of X-ray image of NGC 507 and NGC 499. The lowest contour is 2 σ level (0.4 counts arcmin^{-2} ks^{-1}) and the step size is a factor of 1.585 (0.5 mag interval). The source number of 21 detected small sources is sorted by R.A.

© American Astronomical Society • Provided by the NASA Astrophysics Data System

1995ApJ...441..182K

is in general spherically symmetric, the X-ray isophotes at 2′–3′ are less steep toward the first quadrant (PA = 270°–360°) than that in the other directions.

2.3. *Source Detection and Count Rates*

X-ray count rates for NGC 507 and NGC 499 were extracted from circular regions centered at their X-ray centroids from the background-subtracted, exposure-corrected image (as above). The X-ray centroids are (7668.2, 7622.9) and (8349.2, 9104.9) in pixels and the radii are 1000″ and 300″, respectively (the radius was determined from the radial profiles in § 2.4). All pointlike sources detected in the observed field (described below) are excluded if they are within these radii. We obtain 17627 ± 196 counts and 5813 ± 82 counts for NGC 507 and NGC 499, respectively.

The SASS detection method found more than 100 sources. But it often found multiple detections for many sources particularly near the center of NGC 507 and NGC 499 probably because of the presence of the diffuse extended emission. A different method was followed to determine the existence of individual sources. To detect sources, we first generated an error map, which gives the statistical errors corresponding to the smoothed map. By dividing the smoothed map by the error map pixel by pixel, we then generated a signal-to-noise ratio (S/N) map. We selected sources at above 5 σ in several 15″ × 15″ pixels by eye-examining this S/N map. In this way we find 21 sources. The X-ray positions of these 21 sources are listed in R.A. order in Table 2. These sources are marked in Figure 4 with their source numbers taken from Table 2. All the sources we detect were also found by the SASS method except for source 1, which is partly hidden by the detector support structure.

Recently, Prestwich et al. (1994) and White et al. (1994) pointed out that the filamentary features in A2029 found with the *ROSAT* HRI by Sarazin, O'Connell, & McNamara (1992a) may be not real and caused by applying an inadequate analysis technique. These filaments in A2029 are small-scale features ($\lesssim$10″) in the central 30″ region with strong diffuse emission and White et al. (1994) suggested that these may have been resulted by a circularly symmetric modeling of the elliptically shaped diffuse emission. However, the White et al. (1994) approach, while explaining away the filaments in A2029, is not necessarily a unique representation of the astrophysical object. In our case, we detect a number of prominent pointlike sources, far away from the central (almost circular) halo. It is very hard to imagine how these could be produced by projection effects. Furthermore, the average PSPC spectrum of these sources differs from that of the surrounding emission (§ 2.5.2), proving that our detected sources are not produced by an artifact of data analysis.

The count rate for each source is extracted from the circle centered on the source. The diffuse emission relevant to that position is then subtracted from the source counts. The count rate of the diffuse emission and its error were estimated using the radial profile at a given radius (see § 2.4). For sources 19 and 21 (at 28′ and 42′ away from the center), background counts extracted from the annuli surrounding the sources were subtracted from the source counts. The results are summarized in Table 2. Within the PSPC position uncertainty, these sources do not match with any known SIMBAD object except for sources 2 and 21. A star, HD 8216, and a galaxy, Z0119.4+3300, are within 1.′4 and 1.′3 from source 2. A galaxy, EQ 0123+328, is within 3.′4 from the center of source 21 (its source size $\simeq$5′). We will discuss the possible nature of these sources in § 4.

TABLE 2

OTHER SOURCES

Source Number	*X* Pixel	*Y* Pixel	Radius	Source[a] Count Rate	Diffuse Emission[a] Count Rate	Net[a] Count Rate	Net Error[a] Count Rate	fx[b]
1[c]	10219.70	6997.40	90″	7.94	1.01	6.93	1.28	0.94
2[c]	9981.20	7685.90	90	11.07	1.26	9.81	1.30	1.34
3[c]	9598.10	8046.20	90	7.49	1.72	5.77	1.13	0.79
4	9398.00	7733.30	60	3.60	0.98	2.61	0.71	0.36
5	9366.20	7307.90	90	6.60	2.11	4.49	1.00	0.61
6[c]	9196.10	6058.10	120	24.44	2.47	21.98	1.96	3.00
7	8629.70	8522.60	60	7.45	1.54	5.91	0.85	0.81
8	8440.10	7637.00	60	5.45	3.92	1.53	0.77	0.21
9	8371.40	8155.70	60	6.56	3.28	3.28	0.83	0.45
10	8343.20	7119.20	90	20.32	7.81	12.51	1.45	1.71
11	8028.80	8307.80	60	7.08	3.98	3.10	0.84	0.42
12	8025.50	8865.50	60	8.14	1.44	6.70	0.86	0.91
13	7508.60	8918.00	60	4.81	1.63	3.18	0.74	0.43
14	7273.40	8628.50	60	4.87	2.07	2.81	0.72	0.38
15	7023.20	6724.40	60	4.57	2.19	2.38	0.72	0.32
16	6895.40	7208.00	60	5.28	3.25	2.03	0.76	0.28
17	6887.60	8434.70	60	5.79	2.08	3.71	0.78	0.51
18	6625.40	6462.20	90	5.93	2.55	3.37	0.96	0.46
19[c]	6387.20	4544.60	180	106.78	2.83	103.95	3.93	14.18
20	6217.40	6906.50	90	6.83	2.44	4.39	1.00	0.60
21	2700.50	6720.50	300	215.14	1.40	213.74	5.45	29.15

[a] Count rate are in units of counts ks^{-1}. The diffuse emission is subtracted from the source counts. Its count rate and error were estimated using the radial profile at a given radius (see § 2.4). For sources 19 and 21, background counts extracted from the annuli surrounding the sources were subtracted from the source counts.

[b] Flux was calculated by assuming $T = 0.5$ keV and $N_H = 5.3 \times 10^{20}$ cm^{-2} and is in units of 10^{-13} ergs s^{-1} cm^{-2}.

[c] Sources 1, 2, 3, 6, and 19 are partly hidden by the detector structure.

© American Astronomical Society • Provided by the NASA Astrophysics Data System

1995ApJ...441..182K

2.4. *Surface Brightness Distribution–Radial Profiles*

2.4.1. *NGC 507*

Assuming circular symmetry, we derived a radial profile of the X-ray surface brightness measured in concentric rings centered on the X-ray centroid. Regions of NGC 499 (radius = 300″) and all the detected sources (radii and centers from Table 2) were excluded. Due to the serious position uncertainty at the lowest PI channels, known as the electronic ghost effect (Plucinsky et al. 1993), we used only PI channels above 20, which corresponds to 0.2 keV. However, the radial profile is almost the same as that with all channels in our case. Due to the recent report of the ghost effect which may affect up to PI channel 25 (Fabbiano, Kim, & Trinchieri 1994), we also derived a profile with PI channels above 27 but the results are exactly the same. We also tried nonuniform radial bins to make a signal-to-noise ratio at each radial bin similar, but the results again do not differ greatly. The radial profile is shown in Figure 5*a*. The emission is extended at least out to 1000″. We fitted the observed radial profiles ($r < 1000''$) to the analytic King approximation model, $\Sigma_X \sim [1 + (r/a)^2]^{-3\beta+0.5}$, after convolving this model with the PSPC point response function appropriate for a 1 keV source. The best-fit parameters and 90% confidence regions (in parentheses) are: core radius, a = 39″.7(37″.6–42″.5) and slope, β = 0.449 (0.445–0.457). Given the ~25″ spatial resolution of the PSPC, the estimate of the core radius is very uncertain. However, the power-law slope outside the core radius can be relatively well determined from the emission outside the core region. Where $r \gg a$, the X-ray emission falls as $\Sigma_X \sim r^{-1.69(1.67-1.74)}$.

This best fit is not acceptable, yielding $\chi^2 = 116$ for 29 degrees of freedom. The fit residuals (Fig. 5*a*) show departures of the observed data from the model at r = 90″–150″ (too high), at r = 150″–350″ (too low) and at r = 450″–650″ (too high again). The most significant is the bump at r = 450″–650″. To search for substructures in this radius range, we derived a ratio map by dividing the image by a model image generated with the best-fit radial profile (Fig. 6). Indeed many small clumps are seen in this region, implying that the bump at r = 450″–650″ is likely to be due to the faint sources below the detection threshold. To confirm that the excess emission in this bump is not localized to a particular part of the image, we divided the region into four angular sectors (four quadrants) and regenerated radial profiles for each angular bin. The bump exists in all four bins. It appears strongest in the first quadrant (P.A. = 270°–360°) and weakest in the fourth quadrant (P.A. = 180°–270°). In the first quadrant, there may exist enhanced diffuse emission between NGC 507 and NGC 499 (see Figs. 4 and 6). However, the best-fit parameters of a radial profile obtained by excluding the first quadrant remain within the estimated error.

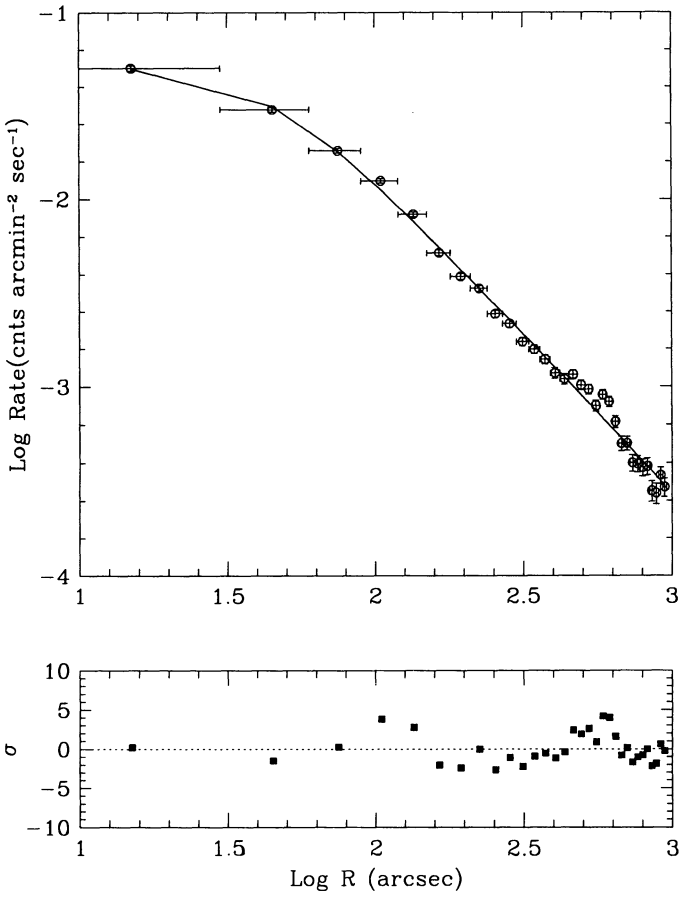

FIG. 5*a*

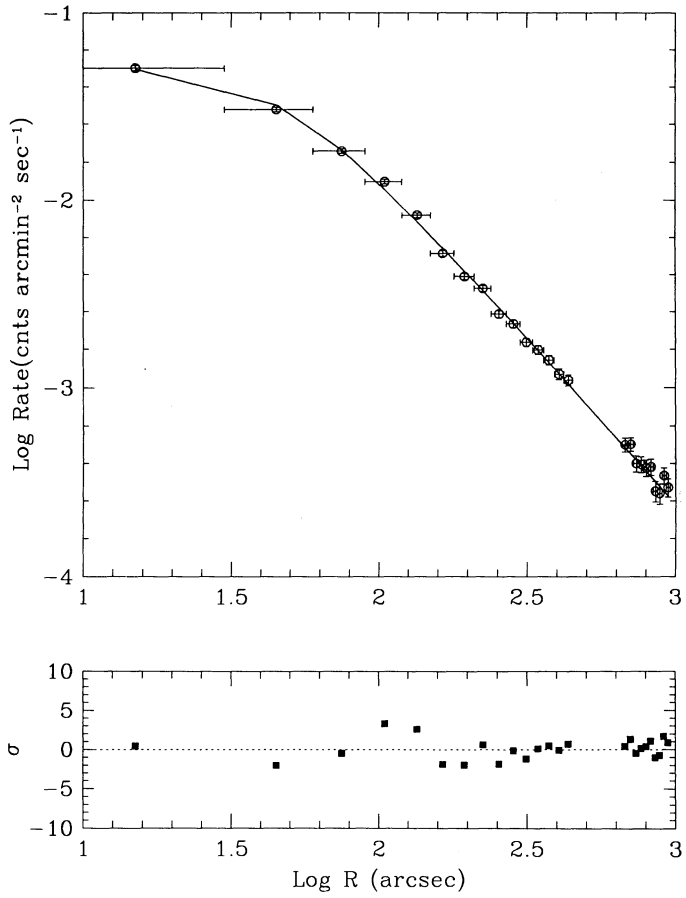

FIG. 5*b*

FIG. 5.—Radial profiles of NGC 507 X-ray surface brightness. (*a*) Radial profile was made excluding NGC 499 and all the sources in Table 2, and the data at $r < 1000''$ was fitted to $\Sigma_X \sim [1 + (r/a)^2]^{-3\beta+0.5}$, and (*b*) same as (*a*) but fitting is to the data at r = 0–450″ and r = 650″–1000″.

© American Astronomical Society • Provided by the NASA Astrophysics Data System

1995ApJ...441..182K

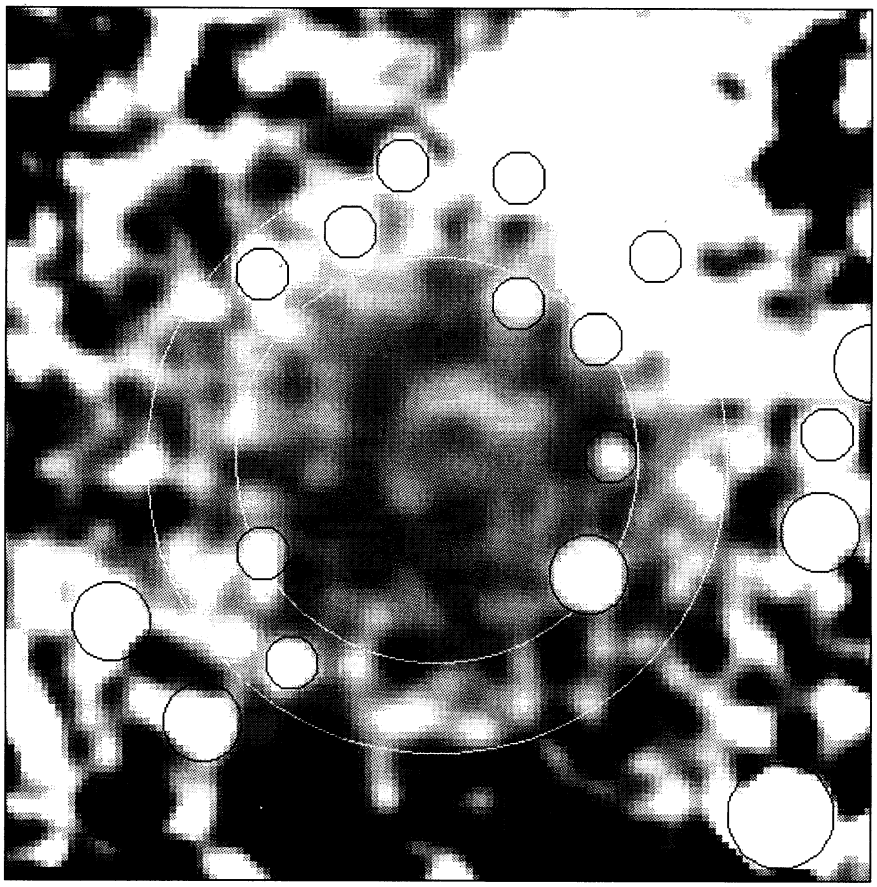

FIG. 6.—A model image was made by the best-fit radial profile of NGC 507 and the image was divided by this model image, then smoothed with a Gaussian $\sigma = 30''$. The small circles mark detected sources and the large annulus indicates the region ($r = 450''$–$650''$) where the excess emission is seen.

We fitted the profile of the region $r = 0''$–$450''$ and $r = 650''$–$1000''$ to exclude the bump. The best-fit slope is $\beta = 0.461$ (0.454–0.469), which corresponds to $\Sigma_X \sim r^{-1.77(1.72-1.81)}$. Such a flat radial profile is also found in the *ROSAT* observations of NGC 4636 (Trinchieri et al. 1994) and NGC 1399 (Kim et al., in preparation). $\Sigma_X \sim r^{-2}$ is excluded at the 99% level. $\Sigma_X \sim r^{-2}$ was suggested to be the typical surface brightness profile of X-ray bright ellipticals from the analysis of the *Einstein* data, although the *Einstein* range encompasses $\Sigma_X \sim r^{-(1.4-2.6)}$ (e.g., Trinchieri et al. 1986; Fabbiano 1989). The minimum χ^2 is significantly reduced to 44 for 22 degrees of freedom and even the observed data at the outer region ($r = 650''$–$1000''$) are well reproduced by the model. The major differences are at the $90''$–$120''$ and $120''$–$150''$ bins which contribute $\chi^2 = 18$ (see Fig. 5*b*).

To explore energy dependencies of the surface brightness distribution, we derived radial profiles for two different energy bands: 0.2–1.0 keV and 1.0–2.4 keV. This choice of energy bins divides the counts roughly in half. Proceeding as above, we find that the acceptable parameter ranges for the soft and hard energy bins are clearly disjoint at the 99% level (Fig. 7). The soft energy radial profile (the best fit is $\beta = 0.442$ for the whole region and 0.454 for the region excluding $r = 450''$–$650''$) is flatter than the hard energy profile ($\beta = 0.461$ for the whole region) and 0.472 for the region excluding $r = 450''$–$650''$). The 90% confidence intervals on the best-fit core radius are $34''$–$37''$ for the soft energy and $48''$–$51''$ for the hard energy, indicating that the soft X-rays are more centrally concentrated than the hard X-rays.

This finding is not affected by the energy-dependent point response function (PRF) and energy-dependent exposure map

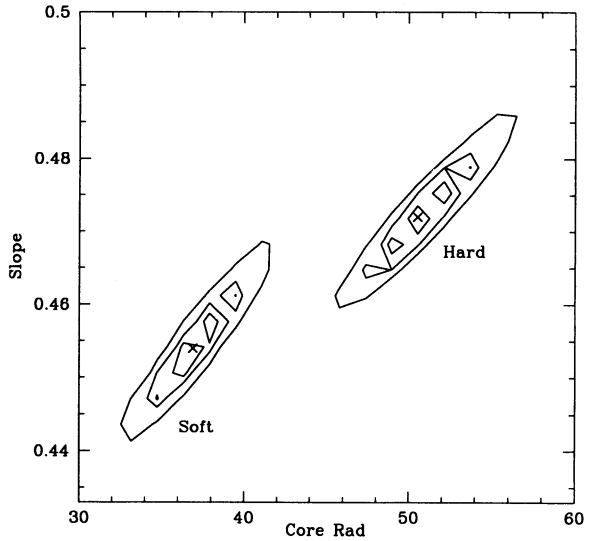

FIG. 7.—Contour plot of acceptable parameter ranges for the radial profiles of soft and hard X-rays. The contours are at the 66%, 90%, and 99% confidence levels.

© American Astronomical Society • Provided by the NASA Astrophysics Data System

1995ApJ...441..182K

(vignetting effect). We checked the PRF effect by reestimating the best-fit parameters using a 0.5 keV PRF for the soft band and a 1.5 keV PRF for the hard band instead of a 1 keV PRF. We also checked the vignetting effect by generating exposure maps at seven different energy bands (Snowden et al. 1994) and applying each exposure map separately to a given energy band. Both effects cause the observed difference between the soft and hard energy band to be even stronger but do not change the results more than the error of our estimates. As remarked in § 2.1, uncertainties in the background subtraction will not affect our results appreciably. In summary, the radial profile of the surface brightness is a function of energy in such a way that the softer X-ray photons are concentrated in the center more strongly and fall less steeply in the outskirts. This is also consistent with the spectral fitting results (§ 2.5).

2.4.2. *NGC 499*

In a similar fashion, we made a radial profile of the X-ray surface brightness of NGC 499, using concentric rings centered on its X-ray centroid and excluding sources 7 and 12. We again used PI channels between 20 and 240. The X-ray emission in NGC 499 is extended to $\sim 300''$. As done for NGC 507, we fitted the King approximation model to the observed data. The best-fit model (Fig. 8) yields $\chi^2 = 8.3$ for 7 degrees of freedom with $\beta = 0.60$ (0.58–0.63) and core radius $= 42''.9$ (39–46). The radial distribution of the X-ray emission is much steeper than that of NGC 507 ($\Sigma_X \sim r^{-2.6}$ at $r \gg a$ in NGC 499). A similar steep X-ray surface brightness distribution was found in NGC 4649 with the *Einstein* IPC (Trinchieri et al. 1986).

2.5. *Spectral Analysis*

To extract the net source counts for the spectral analysis, we also need to subtract the field background. However, we cannot use the method of § 2.1, because the vignetting is a function of energy. Therefore, we have first determined background counts for each spectral channel from source-free regions not hidden by the detector supporting structure, at 30′–40′ from the field center. Then we have applied energy-dependent vignetting corrections to these counts, before subtracting them. Particle background was subtracted separately but its contribution is very small. We tried different background regions, and we found that the uncertainty in the background could only affect our results in determining the absorbing column density for the outer region of the NGC 507 emission (see also Trinchieri et al. 1994).

We used the IRAF/XRAY spectral software package, which bins the 256 pulse height channels into 34 channels. To fit the observed spectra to models, we used the Raymond thermal gas emission model (a revised version of Raymond and Smith 1977) and the Morrison & McCammon absorption model (1983). We also used XSPEC for an independent check of the results and to be able to add together low-energy channels with low statistics. The two software packages produce slightly different results but they are consistent within the error ranges when their abundance tables are adjusted to have the same value.

2.5.1. *NGC 507*

The spectral distribution of the background-subtracted counts extracted from a circle with $r = 1000''$ containing NGC 507 (after excluding NGC 499 and the detected sources listed in Table 2) shows a strong peak at ~ 1 keV (Fig. 9), indicating that the emission is mainly from thermal emission lines. This spectrum, however, cannot be fitted with a single temperature Raymond model with low-energy absorption and 100% cosmic abundance ($\chi^2 = 63$ for 21 degrees of freedom). A similar result was found by Trinchieri et al. (1994) for NGC 4636.

As was done in NGC 4636, we divided the emitting region into several concentric rings to determine if there are radial changes in the spectral parameters. NGC 499 and other

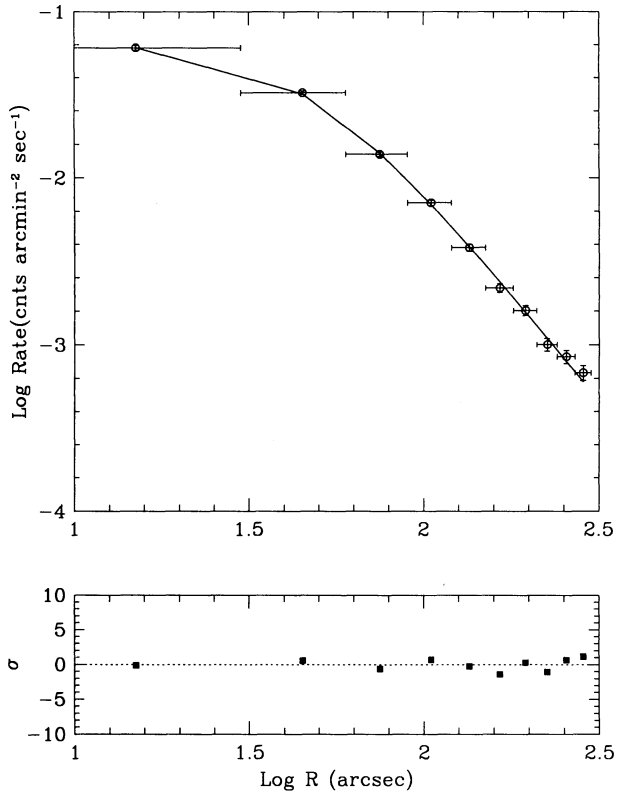

FIG. 8.—Radial profiles of NGC 499 X-ray surface brightness

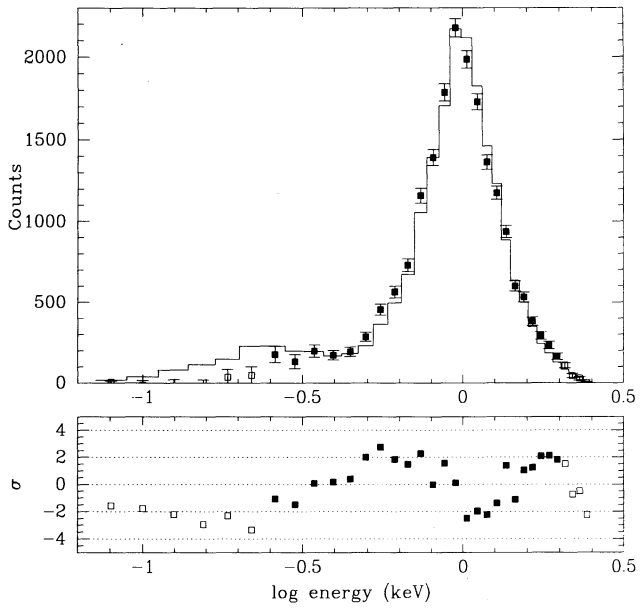

FIG. 9.—Spectral fit of the whole region of NGC 507 ($r < 1000''$) with a single-temperature model with cosmic abundance.

© American Astronomical Society • Provided by the NASA Astrophysics Data System

1995ApJ...441..182K

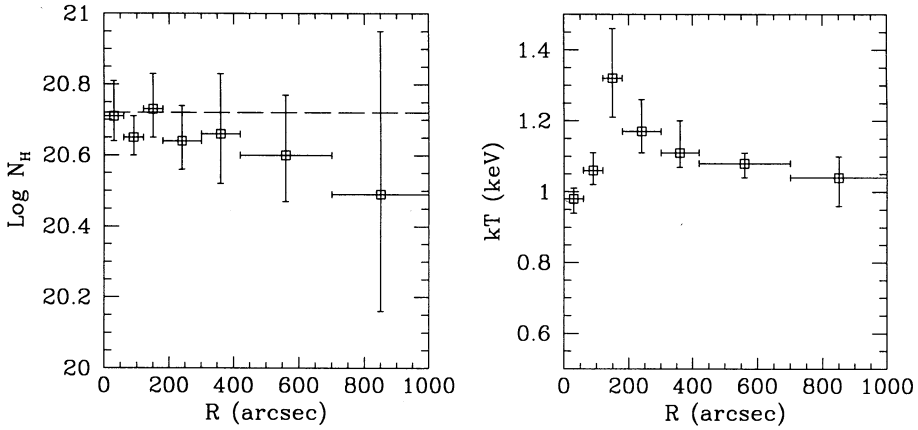

FIG. 10.—Best-fit kT and N_H for various radial bins. The error bars are at the 90% confidence level.

sources in Table 2 were excluded as above. The results of the fit to a single-temperature Raymond model with 100% cosmic abundance (Allen 1973) are listed in Table 3 and the best-fit parameters and their ranges at the 90% level (for two interesting parameters, Avni 1976) as a function of radius are shown in Figure 10. The spectral fits of the subregions are statistically acceptable with reduced χ^2 close to 1. The two innermost radial bins have the highest reduced χ^2 of ~ 1.4. On the average, the emission temperature is close to ~ 1 keV (0.9–1.4 keV) as seen in other X-ray bright elliptical galaxies (Kim, Fabbiano, & Trinchieri 1992; Trinchieri et al. 1994) and the absorption column density is close to the Galactic line-of-sight value (see Table 1).

The emission temperature increases from the center to the 2′–3′ bin (from 1 to 1.3 keV). The temperature difference between the first and third radial bin is significant at 3.5 σ. After 3′, the temperature appears to decrease, but the decrease is marginally significant (about 2 σ). These results are consistent with the energy dependence of the surface brightness radial profile discussed in § 2.4, which shows a smaller core radius and a flatter radial slope for the lower energy range.

The absorbing column density remains constant out to 5′ and similar to the Galactic line-of-sight value, 5.3×10^{20} cm^{-2}, or log $N_H = 20.72$ (Stark et al. 1992). The column density appears to decrease after 5′ but is consistent with the Galactic value within the 90% error.

We tried fitting the data with a two-component Raymond spectrum and with a single-component spectrum, leaving the abundance free to vary. The fitting parameters are given in Table 4. In both instances we do not find appreciably better values of χ^2 and the radial dependence of kT seen in Figure 10 remain the same. The metal abundance is not well constrained with these data. It may be lower than solar (down to $\sim 30\%$) but the acceptable range does not exclude solar abundance. The data only constrain the abundance not to be much higher than the solar value.

2.5.2. *Pointlike Sources*

Near the edge of the X-ray–emitting region of NGC 507 we have detected 19 sources. Sources 19 and 21 are far from NGC 507 ($r \gtrsim 30'$) and may be not related with it. We tried to see if these sources have different spectral properties from those of the diffuse emission surrounding them. Since these sources are weak, we co-added their spectra by summing the counts in each spectral channel to increase the statistical significance (we exclude source 1, 2, 3, and 6 because they are partly hidden by the detector structure). The combined spectrum still contains emission from the extended gas in NGC 507 as well as the emission from the sources. This composite spectrum is compared with that of the diffuse emission from the $r = 420''$–$700''$ radial bin in Figures 11*a* and 11*b*. The best-fit model prediction for the radial bin $r = 420''$–$700''$ (from Table 3) is plotted as a solid line in both figures. It is clear that this model (with normalization as a free parameter) cannot fit the combined spectrum of the point sources, yielding $\chi^2 = 66$ for 24 degrees of freedom (Fig. 11*b*). This point source spectrum definitely contains excess emission at the low energies, indicating that the sources have softer spectral property than the surrounding diffuse gas.

Assuming that the spectrum at $r = 420''$–$700''$ is representative of the diffuse emission, we subtract this spectrum from that

TABLE 3

SPECTRAL PARAMETERS (1T FIT)

Region	Channel Used	log N_H (90%) (cm^{-2})	kT (90%) (keV)	χ^2	Degrees of Freedom
0–60	5–30	20.71 (20.64–20.81)	0.98 (0.94–1.01)	32.40	23
60–120	5–30	20.65 (20.60–20.71)	1.06 (1.02–1.11)	31.93	23
120–180	5–30	20.73 (20.65–20.83)	1.32 (1.21–1.46)	17.93	23
180–300	6–30	20.64 (20.56–20.74)	1.17 (1.11–1.26)	25.60	22
300–420	5–30[a]	20.66 (20.52–20.83)	1.11 (1.07–1.20)	23.72	19
420–700	6–30[b]	20.60 (20.47–20.77)	1.08 (1.04–1.11)	22.75	20
700–1000	7–30[c]	20.49 (20.16–20.95)	1.04 (0.96–1.10)	14.29	18

[a] Channels 5, 6 and 7, 8, 9, 10 are combined.
[b] Channels 6, 7, 8 are combined.
[c] Channels 8, 9, 10, 11 are combined.

© American Astronomical Society • Provided by the NASA Astrophysics Data System

1995ApJ...441..182K

TABLE 4

A. Two-Component Fit[a]

Region	log N_H (cm^{-2})	kT Primary	kT Second	Norm[b]	χ^2	Degrees of Freedom
Adding a Hard Component (1.5–3.0 keV)						
0–60	20.73	0.95	3.00	−0.50	30.47	21
60–120	20.69	0.95	2.99	0.11	18.38	21
120–180	20.76	0.86	1.52	1.13	15.54	21
180–300	20.69	1.05	3.00	0.11	17.49	20
300–420	20.49	0.89	1.51	0.54	14.54	16
420–700	20.52	0.95	2.95	0.07	12.31	18
700–1000.....	20.23	0.99	2.62	−0.57	11.73	14
Adding a Soft Component (0.1–0.5 keV)						
0–60	20.72	0.98	0.46	−2.00	32.40	21
60–120	20.68	1.13	0.49	−1.32	26.22	21
120–180	20.74	1.32	0.10	−2.00	18.00	21
180–300	20.70	1.19	0.23	−1.41	22.16	20
300–420	20.50	1.21	0.45	−1.26	13.52	16
420–700	20.51	1.13	0.45	−1.21	13.41	18
700–1000.....	20.23	1.03	0.25	−1.94	11.61	14

B. With Varying Abundance

Region	log N_H (90%)[c] (cm^{-2})	kT (90%)[c] (keV)	Abundance (90%)[c]	χ^2	Degrees of Freedom
0–60	20.71 (20.43–20.88)	1.01 (0.94–1.07)	0.99 (0.45–)	32.13	22
60–120	20.74 (20.61–20.86)	1.08 (1.02–1.12)	0.53 (0.29–1.00)	23.38	22
120–180	20.77 (20.63–20.95)	1.35 (1.17–1.55)	0.70 (0.31–1.52)	16.68	22
180–300	20.76 (20.61–20.93)	1.14 (1.09–1.30)	0.47 (0.26–0.95)	18.24	21
300–420	20.80 (20.58–21.10)	1.09 (0.96–1.18)	0.37 (0.12–0.98)	18.14	18
420–700	20.76 (20.56–21.05)	1.05 (0.94–1.11)	0.38 (0.16–0.84)	14.67	19
700–1000.....	20.55 (–21.24)	1.04 (0.87–1.11)	0.73 (0.14–)	14.03	17

[a] In two-component model fitting, the acceptable ranges are not well determined.
[b] Logarithm of the relative normalization to the first component.
[c] 90% confidence range with three interesting parameters.

of Figure 11*b*, after normalizing it to match its extraction area to the total point source extraction area. This assumption is reasonable because the spectra of the last three radial bins do not differ significantly from each other (see Table 3). We also used a spectrum taken from source-free regions close to each source (having the same area as the source region) and we reached similar results. The net spectrum after subtracting the diffuse emission is shown in Figure 11*c*. This spectrum is soft and is similar to that of ellipticals with the lowest L_X/L_B (Kim et al. 1992; Fabbiano et al. 1994). As found by Fabbiano et al. (1994), this spectrum can be fitted either with a thermal gas model with a low abundance or a two-temperature gas model with 100% solar abundance. In Figure 11*c*, the best-fit low abundance model is plotted as a solid line. The best-fit parameters are $kT = 0.52$ (0.28–0.86) and abundance = 0 (0.0–0.2) solar, yielding $\chi^2 = 6.7$ for 9 degrees of freedom. The parameters of the two-component model are not well constrained. A model with $kT_1 = 0.1$–0.5 keV and $kT_2 > 1$ and with similar fluxes from the two components fits well the spectrum.

2.5.3. *NGC 499*

The results of spectral fitting to the NGC 499 data are summarized in Table 5. The emission from the whole NGC 499 ($r < 300''$) is not compatible with a single-temperature fit with 100% solar abundance, resulting in a best fit $\chi^2 = 47.6$ with 23 degrees of freedom. To explore radial changes in the spectral properties as seen in NGC 507, we extract spectral data from regions with $r < 2'$ and $r = 2'$–$5'$. When these data are analyzed we find that the temperature decreases toward the center, as seen in NGC 507. The best-fit column density is consistent with the Galactic line-of-sight value. If the abundance is allowed to vary, the minimum χ^2 value are somewhat reduced in the central bin, where the abundance is constrained to be 18%–60% solar. A similar lower value of χ^2 in the central bin is achieved by allowing the presence of two different temperature components with solar abundance.

2.6. *Fluxes and Luminosities*

The X-ray fluxes of NGC 507 and NGC 499 were calculated for each radial bin used for the spectral analysis with the appropriate best fit kT and N_H (Tables 3 and 5). In the energy range of 0.1–2.4 keV, $F_X = 1.3 \times 10^{-11}$ ergs s^{-1} cm^{-2} within $r < 1000''$ for NGC 507; $F_X = 4.0 \times 10^{-12}$ ergs s^{-1} cm^{-2} within $r < 300''$ for NGC 499. The total X-ray luminosity of NGC 507 (adopted distance is 94.5 Mpc) is 1.45×10^{43} ergs s^{-1}, which makes this galaxy one of the X-ray brightest early-type galaxies and comparable to poor clusters. The X-ray luminosity of NGC 499 is 5.3×10^{42} ergs s^{-1}, lower but in the range of gas-dominated ellipticals (Fabbiano et al. 1989; Kim et al. 1992).

The flux of the point sources is given in Table 2. It was calculated by assuming a Raymond thermal gas model with $T = 0.5$ keV and the Galactic line-of-sight absorption $N_H =$

© American Astronomical Society • Provided by the NASA Astrophysics Data System

1995ApJ...441..182K

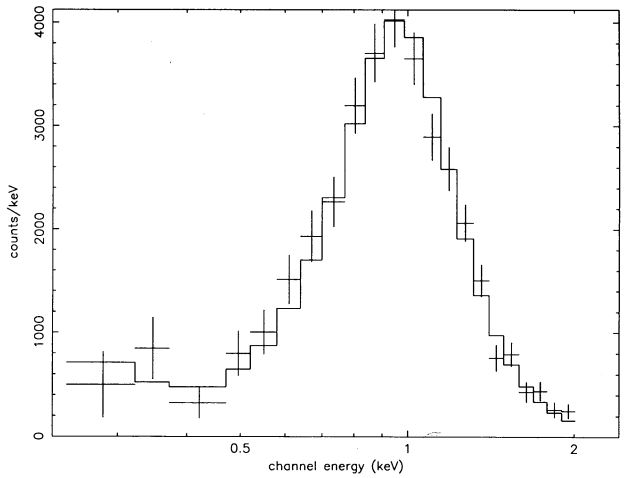

FIG. 11*a*

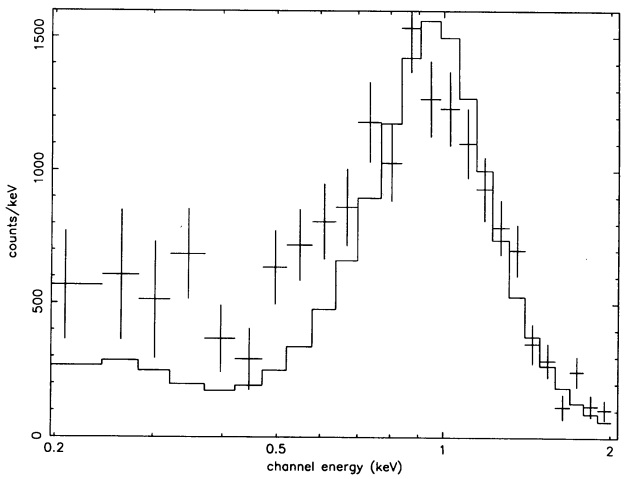

FIG. 11*b*

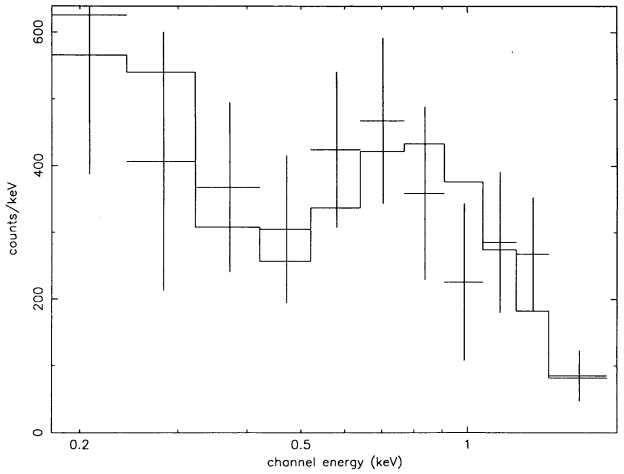

FIG. 11*c*

FIG. 11.—(*a*) Spectrum taken from $r = 420''$–$700''$ and (*b*) combined spectrum taken from the pointlike sources. The solid lines both in (*a*) and (*b*) are the same best-fit model prediction for the spectrum in (*a*). (*c*) Net source spectrum. A normalized diffuse spectrum is subtracted from the source spectrum.

5.3×10^{20} cm^{-2} (Stark et al. 1992). These sources, if they are at the same distance as NGC 507, would have X-ray luminosities of 10^{40}–10^{41} ergs s^{-1}.

3. COMPARISON WITH *EINSTEIN* RESULTS

The NGC 507/499 field was previously observed with the *Einstein* IPC for ~9000 s. The IPC data of NGC 507 and NGC 499 (Fabbiano et al. 1992; Kim et al. 1992) are consistent with the PSPC estimates in terms of the X-ray flux and overall spectral distribution. However, the spectral results of the two observations differ. The most puzzling discrepancy between the two observations is in the measurement of the low-energy absorption. The IPC spectrum (Kim & Fabbiano 1991; see Fabbiano 1993) requires excess absorption over that expected from the Galactic line-of-sight N_H, while the PSPC spectrum (this paper) is consistent with the Galactic value. The two spectra are compared in Figure 12, where the best-fit model predictions for the PSPC data (two-temperature thermal model with $kT_1 = 0.7$ keV, $kT_2 = 1.3$ keV and $\log N_H = 20.7$) are plotted on the data to illustrate the difference. We consider two possibilities: (1) an extra absorbed, hard emission component or (2) an unknown systematic error. There may be a very absorbed, hard emission component (perhaps associated with the active nucleus) which is seen in the IPC observation, but not in the PSPC observation due to the different energy response of the two instruments. This would effectively mimic the excess absorption required by the IPC data. We used various models such as multiple components, edges, and partial covering to imitate such an effect. These complex models considerably reduce χ^2 in the joint fitting but the fit is still not acceptable ($\chi^2 = 48$ for 27 degrees of freedom). Another possibility is that the IPC data are affected by unknown systematics. Fiore et al. (1994) compared *ROSAT* and *Einstein* spectra of a quasar sample and found a systematic discrepancy similar to that in Figure 12. *ASCA* and *AXAF* observations with response up to ~10 keV may resolve the inconsistency. For the moment, we can conclude only that no excess absorption is required to explain the *ROSAT* PSPC data.

4. DISCUSSION

The intensity and extent of the X-ray emission of NGC 507 and NGC 499 and their spectral properties strongly argue for a centrally cooling, hot extended halo. Both emission components from stellar sources in NGC 507 and NGC 499 (see, e.g., Kim et al. 1992) and X-ray emission from the active nucleus of NGC 507 (Fanti et al. 1987; we assume a typical X-ray–radio ratio, see Fabbiano et al. 1989) would not be detected with our data.

Although we are fairly confident of the radial behavior of the temperature of the X-ray–emitting gas in both cases, our measurements cannot set very strong constraints on the metal abundance of this medium, although solar values are allowed. There is a basic uncertainty in the interpretation of PSPC spectra (see Fabbiano et al. 1994 and Trinchieri et al. 1994), which do not permit a unique choice of emission model. Only in the inner regions of both NGC 507 and NGC 499, a thermal gas model with low abundance can reproduce the observed spectra slightly better (slightly reduced minimum χ^2) than the model with solar abundance. However, a similar good fit can be obtained with two-temperature thermal models with solar abundance. To accurately measure abundance (without ambiguity of model dependency), a high spectral resolution obser-

© American Astronomical Society • Provided by the NASA Astrophysics Data System

1995ApJ...441..182K

TABLE 5

A. Spectral Parameters (NGC 499)

Region	Channel Used	log N_H (90%) (cm^{-2})	kT (90%) (keV)	χ^2	Degree of Freedom
0–300.....	5–30	20.76	0.81	47.59	23
0–120.....	6–30	20.65 (20.57–20.77)	0.77 (0.74–0.80)	29.90	22
120–300.....	6–30[a]	20.74 (20.51–21.43)	0.92 (0.80–0.99)	19.69	16

B. Two-Component Fit[b]

Region	log N_H (cm^{-2})	kT Primary	kT Second	Norm[c]	χ^2	Degree of Freedom
Adding a Hard Component (1.5–3.0 keV)						
0–120.....	20.74	0.66	1.73	−0.12	12.84	20
120–300.....	20.30	0.89	3.00	−0.08	17.84	14
Adding a Soft Component (0.1–0.5 keV)						
0–120.....	20.77	0.95	0.50	−0.22	16.58	20
120–300.....	20.00	0.99	0.50	−1.14	20.04	14

C. With Varying Abundance

Region	log N_H (90%)[d] (cm^{-2})	kT (90%)[d] (keV)	Abundance (90%)[d]	χ^2	Degrees of Freedom
0–120.....	20.86 (20.71–21.02)	0.72 (0.67–0.77)	0.29 (0.18–0.60)	14.78	21
120–300.....	20.92 (20.75–21.53)	0.88 (0.81–0.99)	0.46 (0.17–1.63)	16.94	15

[a] Channels 6, 7, 8, 9 and 10, 11, 12 are combined.
[b] In two-component model fitting, the acceptable ranges are not well determined.
[c] Logarithm to the relative normalization to the first component.
[d] 90% confidence range with three interesting parameters.

vation of individual lines which will be provided by *ASCA* and *AXAF* is crucial.

In the following sections, we will discuss the implications of our results for the physical status of the hot interstellar medium (ISM) and for the measurement of the binding masses of NGC 507 and NGC 499. We will also discuss possibilities for the nature of the population of unresolved sources found surrounding NGC 507.

4.1. *Gas Parameters*

To estimate the three-dimensional density distribution of the X-ray–emitting gas, we have used the deprojection scheme described in Kriss et al. (1983). To do this, we implicitly assume that the hot gas is homogeneous, i.e., the physical status of gas in a given radius can be represented by one temperature and density. The deprojected density profile of NGC 507 is shown in Figure 13*a*. To derive this profile the best-fit temperatures determined by the spectral analysis for each annulus (in Table 3) were used. To exclude the bump at $r = 450''$–$650''$, the surface brightness at this radius was interpolated using the best-fit parameters (§ 2.4.1). The solid line is the best-fit model, $n_e \sim [1 + (r/a)^2]^{-1.5\beta}$ with $\beta = 0.463$. This slope is consistent with the radial surface brightness distribution, since the gas temperature does not vary significantly. The shoulder at 90″–

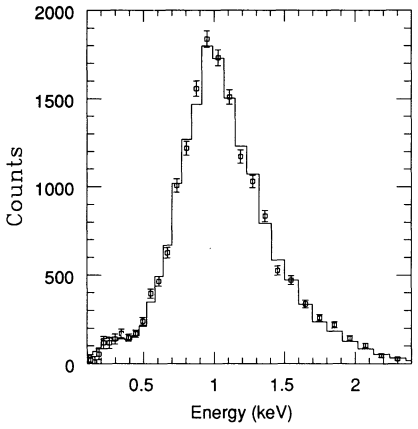

FIG. 12*a*

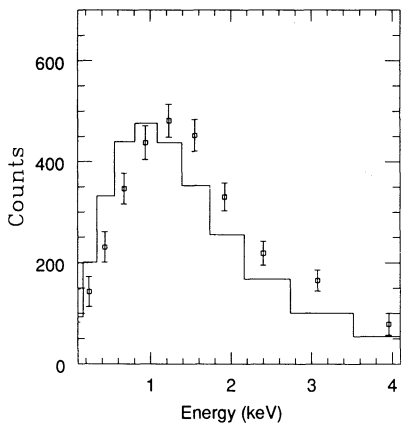

FIG. 12*b*

FIG. 12.—Comparison of (*a*) the *ROSAT* PSPC and (*b*) *Einstein* IPC spectra of NGC 507. The best-fit model for the PSPC spectrum is plotted in both figures.

© American Astronomical Society • Provided by the NASA Astrophysics Data System

1995ApJ...441..182K

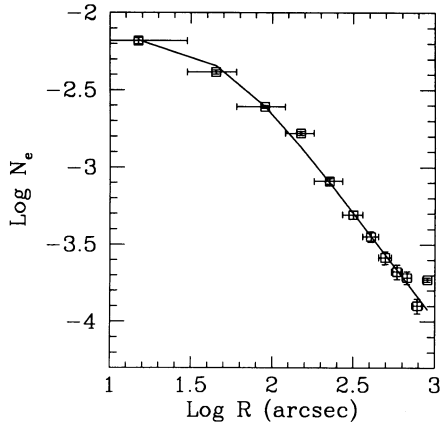

FIG. 13*a*

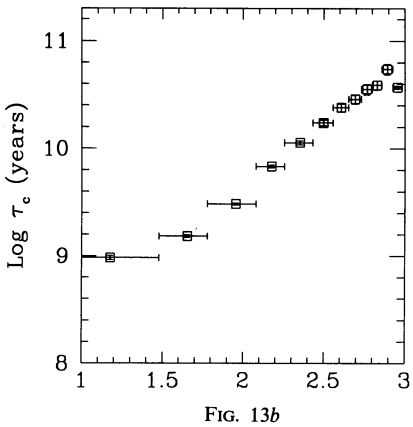

FIG. 13*b*

FIG. 13.—(*a*) Deprojected density profile and (*b*) cooling time as a function of radius. The best-fit temperature at each radial bin is used. The last point in both figures is an artifact of the deprojection routine.

150″ seen in the surface brightness profile (Fig. 5) is even more pronounced in the density profile. This is partly because the temperature at this radius is highest so that the cooling function is lowest.

Using these density and temperature distributions, we estimate the cooling time as a function of radius (Fig. 13*b*). The cooling time is given as $\tau_c = 1.5\ nkT/n_e n_H \Lambda$, where n, n_e, and n_H are the total particle density, electron density, and hydrogen density, respectively, and Λ is the cooling function. The constant is in the range of 1–2.5, depending on its definition (see Sarazin 1988). The cooling time in the center is $\sim 10^9$ yr, smaller than the Hubble time. The cooling radius (i.e., the radius at which the cooling time is equal to the Hubble time, $t_H = 10^{10}$ yr) is ∼200″ (∼92 kpc).

Since the X-ray–emitting gas temperature of NGC 499 does not change greatly as a function of radius, we assume isothermality in this case to estimate the electron density and cooling time. We find that the electron density at the center is $\sim 4 \times 10^{-3}$ cm^{-3} and then falls radially as $\sim r^{-1.8}$. The central cooling time is $\sim 10^9$ yr and the cooling radius is ∼3′ (∼82 kpc).

4.2. *Dark and Visible Mass*

Using the spatially resolved spectra, we have determined temperature and density as a function of radius (Figs. 10 and 13*a*). With these measurements we can derive an accurate estimate of the gravitational mass outside the core region.

To determine the total gravitational mass, we use power-law descriptions for density and temperature gradients which are reasonable approximations in our case in the region well outside the core radius. If we assume $T \sim r^{-\alpha}$ and $N_e \sim r^{-3\beta}$, at a given radius r the binding mass will be given, assuming hydrostatic equilibrium (e.g., Fabricant & Gorenstein 1983), by

$$M_T(M_\odot) = 1.8 \times 10^{12}(3\beta + \alpha)\left(\frac{T}{1\ \mathrm{keV}}\right) \times \left(\frac{r}{10^3\ \mathrm{arcsec}}\right)\left(\frac{d}{10\ \mathrm{Mpc}}\right).$$

Similarly, the mass-to-light ratio scales as

$$\frac{M_T}{L_B} = 1.16 \times 10^{-2} 10^{B/2.5}(3\beta + \alpha)\left(\frac{T}{1\ \mathrm{keV}}\right) \times \left(\frac{r}{10^3\ \mathrm{arcsec}}\right)\left(\frac{d}{10\ \mathrm{Mpc}}\right)^{-1}.$$

In both equations r is the radius within which the mass is determined and T is the temperature of the X-ray–emitting gas at this radius. In these equations we implicitly assume that the external pressure is negligible. Although in absence of a measured radial dependence of T the presence of high external pressure could lead to the erroneous conclusion of the presence of massive dark halos (Vedder et al. 1988; Bertin et al. 1993), this is not the case in NGC 507 because a radial temperature profile has been measured. There is no evidence for an outwardly increasing temperature, which would be appropriate for the model with significant external pressure.

We estimate a mass outside of 3′ where the density and temperature gradients are almost constant and are not seriously affected by the unresolved, cooling core. We take $\beta = 0.461$ (0.54–0.469) from § 2.4 and we determine $\alpha = 0.1$ (0.05–0.2) at $r = 180''$–$1000''$ from Figure 10. The estimated total mass within r, $M_T(<r)$ is shown in Figure 14. The error bars include the errors in temperature and its gradient as well as the error in density gradient. Since the temperature gradient is small, $M_T(<r)$ increases almost linearly as r. The total mass within the outermost radius (1000″) is 2.2×10^{13} (1.8–2.6×10^{13}) $M_\odot$, which corresponds to $M_T/L_B = 97$ (81–113), where L_B includes the optical luminosity of NGC 508. We used $H = 50$ km s^{-1} Mpc^{-1} for the adopted distance. If we used $H = 100$, the mass would be half and the mass-to-light ratio double.

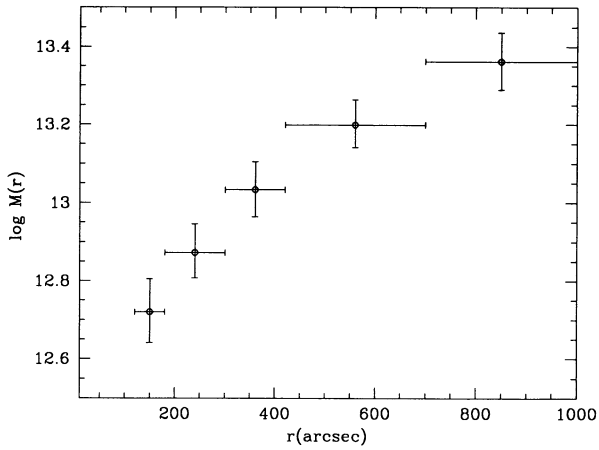

FIG. 14.—Radial dependence of binding mass of NGC 507

© American Astronomical Society • Provided by the NASA Astrophysics Data System

1995ApJ...441..182K

Similarly, to estimate the gravitational mass of NGC 499, we used $T = 0.9$ keV at $r = 300''$, $\beta = 0.62$, and $\alpha = 0$ (i.e., isothermal). The total mass is then 9.5×10^{12} (8.2–11.0×10^{12}) $M_\odot$ within $r = 300''$ (137 kpc) and the mass-to-light ratio is 89 (76–104).

Our estimates indicate large amounts of dark matter in both NGC 507 and NGC 499. If the mass-to-light ratio of stellar matter is 8, the estimated stellar mass of NGC 507 (including NGC 508) is $M(\text{star}) = 1.8 \times 10^{12}\ M_\odot$ which is $\sim 8\%$ of the total mass. The estimated total gas mass of NGC 507 is $\lesssim 2.4 \times 10^{12}\ M_\odot$, $\lesssim 11\%$ of the total mass. For NGC 499, the stellar and gas mass are $\sim 8.5 \times 10^{11}\ M_\odot$ and $\lesssim 2.3 \times 10^{11}\ M_\odot$, which are about 9% and 2% of the total mass, respectively. The gas mass estimated with the X-ray data is an upper limit because we assumed a filling factor of 1. Since the X-ray emissivity depends on a square density, the gas mass for the same X-ray flux can vary largely depending on the unknown volume filling factor ($\sim f^{1/2}$). We will show in § 4.3 and 4.4 that the hot gas may be clumpy within the cooling radius as well as outside the cooling radius. Therefore the above can be used to derive upper limits of the baryonic fraction of $\sim 19\%$ and $\sim 11\%$ in NGC 507 ($r < 458$ kpc) and in NGC 499 ($r < 137$ kpc), respectively.

As it has been frequently noted (for example, see Forman, Jones, & Tucker 1985; Trinchieri et al. 1986), the mass estimated using X-ray data strongly depends on the radius to which X-ray emission can be detected. This radius is $\sim 1000''$ in NGC 507 and two other galaxies with very extended X-ray emission observed with *ROSAT* (NGC 1399 and NGC 5044; Jones et al. 1994 and David et al. 1994), because this radius is just inside the PSPC detector supporting structure (see Fig. 15). The circular PSPC support structure at $\sim 20'$ prevents an accurate estimate of X-ray emission outside this position. Until the background of the PSPC is better understood, the X-ray emission outside the $20'$ circle is very uncertain. The masses quoted in these three studies are almost proportional to the radius quoted. If one estimates the mass within a certain linear distance (say, 100 kpc) from the center, then the masses are almost the same (a few times $10^{12}\ M_\odot$) because all three galaxies have similar gas temperature and their gas is almost isothermal. The different density gradients make the masses different by $\sim 60\%$. Note that the slope of the surface brightness distribution may not directly reflect the binding mass in the case of inhomogeneous cooling flow (see §§ 4.3 and 4.4). If this is the case in NGC 507, an additional uncertainty on the mass measurement is present.

These uncertainties and the uncertainty on the filling factor of the X-ray–emitting gas (which could be clumpy, see §§ 4.3 and 4.4) make very tentative any conclusions based on the baryon fraction of these galaxies. As remarked by Briel, Henry, & Bohringer (1992) and David et al. (1994), baryon fraction $\gtrsim 6\%$ would be inconsistent with $\Omega = 1$, if $\Omega_b h_{50}^2 = 0.05 \pm 0.01$ (Walker et al. 1991). Recent measurement of the deuterium abundance reduces $\Omega_b h_{50}^2$ to 0.02, making the discrepancy more serious (Songaila et al. 1994). David et al.'s (1994) measurement of NGC 5044 and our measurement of NGC 507 suggest larger baryon fractions. However, for the above reasons these measurement are really upper limits (see also Ponman & Bertram 1993).

It is not clear how much of the dark halo of NGC 507 is bound to the galaxy and how much belongs to the galaxy group. The mass estimated by the observed X-ray data is larger than for the typical isolated early-type galaxy, for example, NGC 4636 where the mass-to-light ratio is ~ 30 (Trinchieri et al. 1994). The X-ray luminosity is at the highest end of those of the observed galaxies (Fabbiano, Kim, & Trinchieri 1992) and comparable to those of poor clusters (Kriss et al. 1983). The emission temperature is typical of early-type galaxies and much lower than that of rich clusters (for example, David et al. 1993) and at the lowest end of the poor cluster temperature distribution (Kriss et al. 1983). The almost isothermal temperature gradient is also similar to that of typical elliptical galaxies (e.g., NGC 4636, Trinchieri et al. 1994; NGC 4472, Forman et al. 1993) and is in contrast to a large positive gradient found in clusters, for example, in the Virgo Cluster around M87 (e.g., Fabricant & Gorenstein 1983). The velocity dispersion of the NGC 507 group is about 600 km s^{-1} (Wegner et al. 1993). The virial mass is then $2.5 \times 10^{14}\ M_\odot$ within 1 Mpc. Although the virial mass is uncertain, it is an order of magnitude larger than the mass estimated with the X-ray data. The emission-averaged temperatures of clusters of galaxies are well correlated with their velocity dispersions (Edge & Steward 1991; Lubin & Bahcall 1993), indicating that the hot gas is in hydrostatic equilibrium under the gravitational potential specified by the velocity dispersion. The group velocity dispersion of the NGC 507 group (595 km s^{-1}, Wegner et al. 1993) is far in excess to that expected for its temperature (~ 1 keV) from this relationship (~ 330 km s^{-1} is expected for 1 keV). This may imply that the observed hot gas may be bounded mainly by the galaxy gravitational potential, including the heavy halo. In the outer region, some of the group potential may play a role, but not all the mass in the group seems to work to hold the observed hot gas.

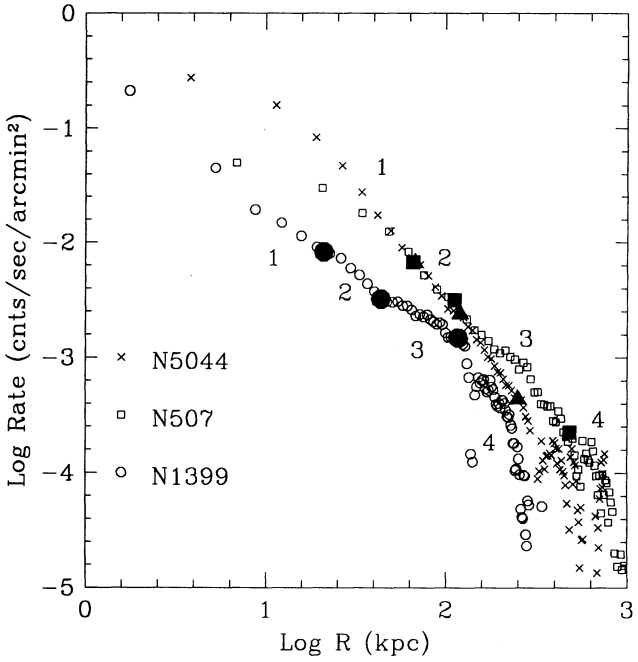

FIG. 15.—Comparison of radial profiles of X-ray surface brightness of NGC 1399 (*open circle*), NGC 5044 (*cross*), and NGC 507 (*open square*). The big filled circles, triangles, and squares indicate positions at $r = 1000''$ from the center (outer set), positions of the cooling radius (middle set), and positions where the measured temperature peaks (inner set) for NGC 1399, NGC 5044, and NGC 507, respectively. The dips at 140 kpc for NGC 1399, 300 kpc for NGC 5044, and 580 kpc for NGC 507 are due to the detector structure.

© American Astronomical Society • Provided by the NASA Astrophysics Data System

1995ApJ...441..182K

4.3. *Implications for Cooling Flow Models*

The temperature decrease toward the center found in NGC 507 (also possibly in NGC 499) is clear evidence that the gas is cooling. Indeed the cooling time in the center of NGC 507 and NGC 499 is $\sim 10^9$ yr, much shorter than the Hubble time. Unless it is being reheated, the gas must flow in.

In the case of homogeneous inflow (i.e., no mass deposition), the hydrodynamic equations can be written as

$$\frac{1}{r^2}\frac{d}{dr}(r^2\rho v) = 0 \text{ (or, } \dot{M} = 4\pi r^2 \rho v) ,$$

$$\frac{dP}{dr} = -\frac{GM}{r^2}\rho ,$$

$$\rho v \frac{dE}{dr} - \frac{P}{\rho} v \frac{d\rho}{dr} = -\rho^2 \Lambda .$$

Here ρ, v, P, and E are the density, flow velocity, pressure, and thermal energy ($3kT/2\mu m_{\rm H}$) of the gas. M is the total binding mass within r and Λ is the cooling function. We assume a steady state condition which is valid within the cooling radius, where the flow time (cooling time) is shorter than the age, i.e., $t_c < t_{\rm H}$. The first equation (continuity equation) mean a constant mass inflow rate, the second one is the equation of hydrostatic equilibrium and the third one is the equation of energy conservation. Since the gas is almost isothermal (which is valid down to the position of the temperature peak), then the energy equation is simply reduced to

$$\frac{P}{\rho} v \frac{d\rho}{dr} = \rho^2 \Lambda ,$$

or, after substituting the pressure gradient with the gravitational potential gradient,

$$\rho v \frac{GM}{r^2} = -\rho^2 \Lambda .$$

This equation simply means that the potential energy gain of the inflowing gas is balanced with the radiative loss by the X-ray emission. If we write the gas density and velocity as $\rho \sim r^{-n}$ and $v \sim r^{n-2}$, making them satisfy the continuity equation, then from the energy equation, $\rho \sim r^{-1.5}$, which corresponds to $\Sigma_X \sim r^{-2}$. This equation is valid in the case of a homogeneous, isothermal, steady state inflow (i.e., inside the cooling radius and outside the region where the temperature is decreasing). Outside the cooling radius, the steady state condition is not valid because the flow time is very large. On the other hand, the assumption of homogeneity and isothermality is not valid in the cooling region where the temperature decreases inward.

Combining the three hydrodynamic equations, one can write the constant mass inflow rate, $\dot{M} = 4\pi r^2 \rho^2 \Lambda / GM/r^2$ (see also eq. [1] of Canizares, Steward, & Fabian 1983). The mass inflow rate at the cooling radius of NGC 507 is $\dot{M} \simeq 40\ M_\odot$ yr^{-1}. Similarly, we can estimate the average cooling rate within the cooling radius by dividing the energy loss rate by the enthalpy of the gas $\dot{M} = (2\mu m_{\rm H} L_X)/(5kT)$, where L_X is the bolometric X-ray luminosity inside the cooling radius. The average cooling rate of NGC 507 is $\sim 35\ M_\odot$ yr^{-1}. The mass inflow rate at the cooling radius of NGC 499 is $\dot{M} \simeq 30\ M_\odot$ yr^{-1} and the average cooling rate is $\sim 20\ M_\odot$ yr^{-1}.

If all the cooling gas is falling into the center, we would have a central peak of the surface brightness much more pronounced than observed. Some of the hot gas will cool locally and drop out of the overall inflow and hence the actual inflow rate inside the cooling radius will become smaller as gas flows toward the center. The local excess at $r = 90''$–$150''$ (41–69 kpc) seen in both surfacce brightness and density of NGC 507 could be an example of the increased local cooling within the cooling radius. High-resolution spectral/spatial observations are necessary to confirm this hypothesis. The detailed process of how mass deposition occurs as a function of radius is not easily determined because a priori knowledge of the distribution of the gravitating mass (i.e., the potential) is needed (Arnaud 1988; see also David et al. 1984). With our data we can determine this well only outside the cooling radius (see Fig. 14 and § 4.2).

To assess how much the potential varies particularly inside the cooling radius, we compare the X-ray surface brightness profile of NGC 507 with those of two other galaxies in poor groups. This comparison suggests that the mass deposition rate and the shape of the potential may vary widely from galaxy to galaxy. These three galaxies (all observed with the *ROSAT* PSPC) are NGC 507, NGC 1399 (Jones et al 1994) and NGC 5044 (David et al. 1994). They are similar in many respects, for example, cluster richness (all three are poor in clusters or galaxy groups), X-ray temperature (all three have $kT \simeq 1$ keV) and central cooling core (all three show temperatures decreasing toward the center). However, their surface brightness distributions differ widely. Beyond the core radius, $\Sigma_X \sim r^{-1}$ in NGC 1399 (Jones et al. 1994) and $\Sigma_X \sim r^{-2.2}$ in NGC 5044 (David et al. 1994), while we find $\Sigma_X \sim r^{-1.8}$ in NGC 507 (§ 2.4.1). The X-ray radial profiles of the three galaxies are compared in Figure 15, where the profiles are plotted against the linear distance from the center (as those authors, we adopted $D = 24$ Mpc and 52.2 Mpc for NGC 1399 and NGC 5044, respectively). We marked with three large, filled symbols in each radial profile the position of the temperature peak, the cooling radius, and the outermost radius ($\sim 1000''$), where the X-ray emission can be accurately measured.

These three positions divide the surface brightness profiles into four subregions: (1) within the temperature peak (down to a few kpc) where the temperature decreases inward, i.e., the cooling gas is mainly deposited; (2) between the point where the temperature stops decreasing and the cooling radius where the assumption of steady state, homogeneous, and isothermal flow may be valid; (3) between the cooling radius and the outermost radius ($\sim 1000''$), where the binding mass can be well determined by the X-ray data; and (4) outside $\sim 1000''$, where the X-ray data are very uncertain.

In region (2), between the temperature peak and the cooling radius, the slopes of the radial profiles are similar. Within this region, the uncertainty in our measurement is such that temperature could be constant, and the gas could still be in cooling flow regime. These slopes are close to $\Sigma_X \sim r^{-2}$ as expected for a homogeneous, isothermal gas flow. However, if there is a real temperature peak (i.e., the temperature is decreasing radially), this result may be just coincidental. In this case, a cooling flow would be restricted only to the region within the temperature peak.

In the region where the gas temperature decreases inward (region 1), the X-ray profiles begin to differ and keep the trend down to a few kpc radius. Inside a few kpc, the PSPC data of NGC 1399, the galaxy closest to us, suggest a change in slope. The *ROSAT* HRI observations of NGC 1399 confirm this

© American Astronomical Society • Provided by the NASA Astrophysics Data System

1995ApJ...441..182K

central peak (Kim et al. 1994). NGC 5044 and NGC 507 may also contain such a central peak which would be unresolved with the *ROSAT* PSPC. HRI observations are required to test this.

It is difficult to interpret the radial profile in region (1) from the position of the temperature peak to a few kpc (excluding the central peak of NGC 1399, because we do not have comparable data for the other two galaxies). If one assumes that the shape of the potential is similar in the three cases, the different X-ray radial profiles may imply that the cooling flow of NGC 1399 deposits mass at large radii while that of NGC 5044 deposits mass mainly at the center; NGC 507 would be an intermediate case. Qualitatively this argument may be correct. However, the exact amount of mass deposition as a function of radius may differ from this simple scenario because the determination of the mass deposition process is closely coupled with the shape of the potential, which we cannot determine with the X-ray data.

Outside the cooling radius (region 3), the gas is not in a steady state because the flow time is much larger than the Hubble time. However, the equation of hydrostatic equilibrium is valid because the sound crossing time of the ~ 1 keV gas is short. This justifies the use of this equation in determining the binding mass in § 4.2. The different slopes of the X-ray radial profiles reflect the difference in the binding mass. However, the gas may not be homogeneous even outside the cooling radius. We will discuss the possibility in § 4.4. Then the different slopes represent mixed effects of different binding masses and inhomegeneities.

The possibility that the potential in region (4) ($r \gtrsim 1000''$), where X-ray data cannot determine a mass, may vary is suggested by a comparison of the optical velocity dispersion of group galaxies in the three cases with the stellar velocity dispersion of each dominant galaxy. The Fornax group where NGC 1399 resides has the lowest group velocity dispersion (~ 325 km s^{-1}; Ferguson & Sandage 1990) while the NGC 507 and NGC 5044 groups have higher velocity dispersions (595 km s^{-1} and 474 km s^{-1}, respectively; Ferguson & Sandage 1990 and Wegner et al. 1993). The ratio of the group velocity dispersion to the galaxy velocity dispersion may be used as a measure of the shape of the potential in the region between the galaxy scale and the group scale. NGC 1399 has the lowest ratio (~ 1) and NGC 5044 has the highest ratio (~ 2) while NGC 507 is intermediate (1.6). A recent measurement using globular clusters confirms the low-velocity dispersion of the NGC 1399 group (Grillmair et al. 1994). Unless the optical measurements are contaminated by nongroup members or the velocity is not isotropic, the wide range of the velocity dispersion ratios indicates that the group velocity dispersion measures the potential in a much larger scale than the outer limit of the gas distribution. To confirm the difference in the shape of the potential in a larger scale suggested by the optical data, X-ray data in such a larger scale are necessary. These may be obtained by better understanding the field background and/or obtaining long off-center exposures of these galaxies.

The X-ray surface brightness of NGC 499 is quite in contrast to those of the three galaxies mentioned above in that its X-ray distribution is very steep ($\Sigma_X \sim r^{-2.6}$). The steepness is at the highest end of those measured with *Einstein* X-ray bright early-type galaxies (see Fabbiano 1989). The hot gas in NGC 499 is likely maintained by the steep galaxy potential (i.e., the potential of the NGC 507 group does not have a significant effect). This is also indicated by the relatively small extent of the X-ray gas. The steep surface brightness distribution of NGC 499 may imply that most of gas is falling toward the center before condensing at a large radius, as suggested by the presence of a possible cool core and the short cooling time at the center. It may also be interpreted as a stripped gas distribution due to tidal interaction with NGC 507.

4.4. *The Unresolved Sources in the Halo of NGC 507*

As discussed in § 2.3 (see Table 2) 19 faint pointlike sources are detected above 5 σ near the edge of the X-ray–emitting gas. The number of sources found in this observation is about twice that expected by chance in the corresponding area of sky with a comparable flux threshold (estimated using deep survey field data by Hasinger et al. 1993), indicating that many of the detected sources are related with NGC 507 or its group.

Except for a few very bright sources (such as sources 6, 10, 19, and 21), the X-ray luminosities of these sources are in the range of 10^{40}–10^{41} ergs s^{-1} assuming they are at the distance of NGC 507. These values are far in excess of those expected for binary stars or globular clusters associated with NGC 507 (e.g., Fabbiano 1989). Their average spectrum is also soft (Fig. 11*c*) in contrast to the hard spectrum expected from X-ray accretion binaries. The composite spectral distribution of these sources is reminiscent of that of elliptical galaxies with the lowest L_X/L_B (Kim et al. 1992; Fabbiano et al. 1994). However, given their luminosities, it is highly unlikely that they could be due to the integrated emission of the soft stellar sources invoked to explain the emission of X-ray faint ellipticals (Fabbiano et al. 1994). With the possible exception of two of them, these sources do not have any obvious optical counterpart (see § 2.3). In this they are similar to otherwise more luminous sources found near the clusters of galaxies A1367 (Bechtold et al. 1983) and A2256 (Henry & Briel 1991).

We speculate that these sources may be cooling clumps in the cooling flow even though they lie outside the cooling radius. A local high-density blob will cool more rapidly than the surrounding gas and the cooler clumps are then dropped out of the general inflow and remain at large radii. The spectral properties of these sources indicate that they are cooler than the diffuse gas at the same radius (Fig. 11). The fainter substructures (see Fig. 6) causing a bump in the radial profile at 450″–650″ (see Fig. 5) may also be due to local cooling. The spectral behavior of the surface brightness (Fig. 7) is in agreement with the hypothesis of mass deposition at large radii. The cooling gas at large radii will produce much stronger soft emission in the outer region (see White & Sarazin 1987b; Vedder et al. 1988; Sarazin & Ashe 1989). This is what our observations suggest, i.e., the radial profile is flatter in the soft energy band (0.2–1.0 keV) than in the hard energy band (1.0–2.4 keV).

It is not clear how density fluctuations are originally introduced into the hot gas and how cooling clumps form and evolve through thermal instability (Balbus & Soker 1989; Loewenstein 1989; see Fabian, Nulsen, & Canizares 1991 for a review). In particular, Balbus & Soker (1989) have shown that the linear thermal instability does not grow and produces just a buoyant oscillation. Fabian et al. (1991) suggested that density inhomogeneities might be initiated by some dynamical effects (such as stripping of gas, winds, infall, etc.). In NGC 507, there is some evidence of dynamical perturbations. Within its optical radius, there is a possible interacting galaxy, NGC 508, at 1.′5 away (5 times less bright than NGC 507). Optical observations of the surface brightness distribution reveal shell features around NGC 507 (Arp 1966; Prugniel, Davoust, & Nieto

© American Astronomical Society • Provided by the NASA Astrophysics Data System

1995ApJ...441..182K

1989), which are often interpreted as evidence of interaction (e.g., Malin & Carter 1983; Schweizer 1990). The density inhomogeneities may also be related to the tidal interaction with NGC 499.

However, these sources look like unresolved point sources rather than like filaments as seen in the central regions of cooling flow clusters, 2A 0335+096 and A2029 (Sarazin, O'Connell, & McNamara 1992a, b). If these sources are cooling clumps, their electron density must be larger than $\sim 10^{-3}$ cm^{-3} for the cooling time to be shorter than the Hubble time. Then the upper limits of their size and mass are ~ 14 kpc and $3 \times 10^8\ M_\odot$. At the distance of NGC 507, the angular size would be $\lesssim 0.5$, therefore it would appear as a pointlike source with the PSPC. High-resolution spatial/spectral observations will be very important to establish if they are cooling clumps.

5. SUMMARY AND CONCLUSIONS

We have observed the field containing NGC 507 and NGC 499 with the *ROSAT* PSPC for a total of $\sim 20{,}000$ s. With this deep observation we have studied in detail the X-ray properties of these galaxies. Our results are summarized below.

1. In both galaxies the L_X/L_B ratio is far higher than that expected from the integrated emission of a population of X-ray–emitting stellar sources, suggesting that the emission is dominated by hot, gaseous components. In both cases the average spectral distribution of the PSPC counts support this conclusion, presenting a very pronounced peak near 1 keV, which can be explained with the blended contribution of thermal line emission. The X-ray halo of NGC 507 is also far more radially extended than its optical stellar emission.

2. We detect a total of 17,600 counts from NGC 507, corresponding to an X-ray flux of 1.3×10^{-11} ergs s^{-1} cm^{-2} with 1000″ (458 kpc) and luminosity of 1.45×10^{43} ergs s^{-1} in the energy range of 0.1–2.4 keV ($D = 94.5$ Mpc).

3. NGC 499 is detected with 5800 counts within 300″ (137 kpc), corresponding to $F_X = 4.0 \times 10^{-12}$ ergs s^{-1} cm^{-2} and $L_X = 5.3 \times 10^{42}$ ergs s^{-1}.

4. The X-ray emission of NGC 507 is extended at least out to 1000″ (458 kpc at a distance of 94.5 Mpc). The surface brightness distribution outside the core region of NGC 507 declines as $\Sigma_X \sim r^{-1.8}$. Both core radius and gradient of the surface brightness are function of energy such that the surface brightness is both more centrally concentrated and flatter at the outer radii for softer rather than harder X-rays.

5. The X-ray–emitting temperature of NGC 507 is near ~ 1 keV but there is clear cooling at the center and possibly at the outer radii. The temperature peaks at a radius of 2′–3′ (55–82 kpc). The absorption column density is consistent with the Galactic line-of-sight value at all radii. We cannot set a strong constraint on the metal abundance of the X-ray–emitting gas. Values ranging from 30% up to 100% of solar value are acceptable. A better definition of the spectral parameters and of emission model will require higher resolution data (see also Trinchieri et al. 1994).

6. We detected 19 weak pointlike sources near the edge of the X-ray–emitting region of NGC 507. Their spectrum is on average softer (~ 0.5 keV) than that of the X-ray emission at a similar radius from the center. Their fluxes are in the range of 10^{-14} to 10^{-13} ergs s^{-1} cm^{-2} and if they are associated with NGC 507, their luminosities are in the range of 10^{40}–10^{41} ergs s^{-1}. The number density of these sources is well in excess to that of the expected background sources, indicating that a good fraction of them ($\sim \frac{1}{2}$) are associated with NGC 507.

7. The surface brightness distribution of NGC 499 is steep ($\Sigma_X \sim r^{-2.6}$), in contrast to that of NGC 507, but in the range of those measured with *Einstein* in X-ray bright early-type galaxies (see Fabbiano 1989). Its emission temperature is also near 1 keV and there is a suggestion of cooler core. The choice of the spectral model is more uncertain than in NGC 507; both a low-abundance model and a two-temperature solar abundance one give a better fit to the core emission. This is reminiscent of the results on NGC 4636 (Trinchieri et al. 1994).

These results suggest the following.

1. Both NGC 507 and NGC 499 contain large amounts of dark matter; total binding masses are $2 \times 10^{13}\ M_\odot$ within 458 kpc and 9×10^{12} within 137 kpc, respectively, yielding $M_T/L_B \sim 100$ in both cases. The baryonic mass (including stellar and gas masses) is $\lesssim 19\%$ for NGC 507 and $\lesssim 11\%$ for NGC 499. The upper limits are due to the unknown volume filling factor of the hot gas which could be clumpy.

2. Both galaxies are experiencing cooling flows. The central cooling time is $\sim 10^9$ yr in both cases, shorter than the Hubble time. The cooling radius is at $\sim 200''$ (~ 92 kpc) in NGC 507 and $\sim 180''$ (82 kpc) in NGC 499. Within the cooling radius, the cooling rate is roughly 30–40 $M_\odot$ yr^{-1} in NGC 507 and 20–30 $M_\odot$ yr^{-1} in NGC 499.

3. By comparing the NGC 507 X-ray surface brightness with those of two other galaxies observed with the PSPC, NGC 5044 and NGC 1399, we find that the surface brightness distributions vary widely in otherwise similar galaxies. Only in the region between the point where the temperature stops decreasing and the cooling radius (where one may assume the isothermal, homogeneous, steady state condition), the radial profiles of the three galaxies are similar to $\Sigma_X \sim r^{-2}$, as expected. This wide variation of radial profiles may indicate significant variation in the mass deposition rate as a function of radius. However, the shape of the potential may vary as well in the cooling regions where X-ray data cannot accurately measure the binding mass (and potential gradient). A comparison of stellar and galaxy velocity dispersions in the three cases also suggest differences in their potentials in the radius range between the galaxy scale and the group scale.

4. We speculate that the unresolved, soft sources are cooling clumps. An excess of the surface brightness distribution seen at $r = 450''$–$650''$ could be due to an unresolved population of similar sources. The inhomogeneous cooling flow may be dynamically affected by the nearby companion galaxies, NGC 508 and NGC 499. The relatively flat radial profile of X-ray surface brightness, and the different slope as a function of energy are consistent with this interpretations. If there is a large number of undetected cooling clumps in a wide range of radii, then the radial profile does not directly represent the potential, and a further uncertainty must be added to the measurement of the binding mass. The presence of cooling clumps could be confirmed by detection of extended emission with high-resolution *ROSAT* HRI observations.

5. The relatively steep distribution of X-ray surface brightness of NGC 499 as well as the relatively small extent of its gas distribution suggests that the hot gas of NGC 499 is trapped by the galaxy potential well, not by the potential of the NGC 507 group. The data could also suggest that the hot gas may be stripped by the tidal force of NGC 507.

© American Astronomical Society • Provided by the NASA Astrophysics Data System

1995ApJ...441..182K

In a following paper, we will describe quantitatively the detailed radial behavior of mass deposition and the shape of the gravitational potential as a function of radius, and discuss their implications for the nature of cooling flows.

This work was supported by NASA grant NAG 5-2152 (*ROSAT*), NAGW 2681 (LTSA), NASA contract NAS 8-39073 (*AXAF* Science Center) and KOSEF international program. We thank Claude Canizares, Martin Elvis, Paul Eskridge, and Glen Mackie for useful discussions and comments.

REFERENCES

Allen, C. W. 1973, Astrophysical Quantities (3d ed.; London: Athlone)
Arnaud, K. A. 1988, in Cooling Flows in Clusters and Galaxies, ed. A. C. Fabian (Dordrecht: Kluwer), 31
Arp, H. 1966, ApJS, 14, 1
Avni, Y. 1976, ApJ, 210 642
Balbus, S., & Soker, N. 1989, ApJ, 341, 611
Bechtold, J., Forman, W., Giacconi, R., Jones, C., Schwarz, J., Tucker, W., & Van Speybroeck, L. 1983, ApJ, 265, 26
Bertin, G., Pignatelli, E., & Saglia, R. P. 1993, A&A, 49, 137
Briel, U. G., Henry, J. P., & Bohringer, H. 1992, A&A, 259, L31,
Canizares, C. R., Fabbiano, G., & Trinchieri, G. 1987, ApJ, 312, 503
Canizares, C. R., Markert, T. H., & Donahue, M. E. 1988, in Cooling Flows in Clusters and Galaxies, ed. A. C. Fabian (Dordrecht: Kluwer), 63
Canizares, C. R., Steward, G. C., & Fabian, A. C. 1983, ApJ, 272, 449
David, L. P., Jones, C., Forman, W., & Daines, S. 1994, preprint
David, L. P., Slyz, A., Jones, C., Forman, W., Vrtilek, S. D., & Arnaud, K. A. 1993, ApJ, 412, 479
de Vaucouleurs, G., de Vaucouleurs, A., Corwin, H. G., Buta, R. J., Paturel, G., & Fouque, P. 1991, Third Reference Catalogue of Bright Galaxies (New York: Springer)
Ebneter, K., Djorgovsky, S., & Davis, M. 1988, AJ, 95, 422
Edge, A. C., & Steward, G. C. 1991, MNRAS, 252, 428
Fabbiano, G. 1989, ARA&A, 27, 87
———. 1993, in Structure, Dynamics and Chemical Evolution of Elliptical Galaxies, ed. I. J. Danziger, W. W. Zeilinger, & K. Kjar (ESO Conf. Proc. No. 45), 617
Fabbiano, G., Gioia, I. M., & Trinchieri, G. 1989, ApJ, 347, 127
Fabbiano, G., Kim, D.-W., & Trinchieri, G. 1992, ApJS, 80, 531
———. 1994, ApJ, 429, 94
Faber, S. M., Wegner, G., Burstein, D., Davies, R. L., Dressler, A., Lynden-Bell, D., & Terlevich, R. J. 1989, ApJS, 69, 763
Fabian, A. C., Nulsen, P. E. J., & Canizares, C. R. 1984, Nature, 310, 733
———. 1991, AA Rev., 2, 191
Fabricant, D., & Gorenstein, P. 1983, ApJ, 267, 535
Fanti, C., Fanti, R., de Ruiter, H. R., & Parma, P. 1987, A&AS, 69, 57
Ferguson, H. C., & Sandage, A. 1990, AJ, 100, 1
Fiore, F., Elvis, M., McDowell, J. C. Siemiginowska, A., & Wilkes, B. J. 1994, ApJ, in press
Forman, W., Jones, C., David, L., Franx, M., Makishima, K., & Ohashi, T. 1993, ApJ, 418, L55
Forman, W., Jones, C., & Tucker, W. 1985, ApJ, 293, 102
Grillmair, C. J., Freeman, K. C., Bicknell, G. V., Carter, D., Couch, W. J., Sommer-Larsen, J., & Taylor, K. 1994, ApJ, 422, L9
Hasinger, G., Burg, R., Giacconi, R., Hartner, R., Schmidt, M., Trumper, J., & Zamorani, G. 1993, A&A, 275, 1
Henry, J. P., & Briel, U. G. 1991, A&A, 246, L14
Jones, C., Stern, C., Forman, W., Breen, J., David, L., Tucker, W., Franx, M., & Fabian, A. C. 1994, preprint
Kim, D.-W., & Fabbiano, G. 1991, BAAS, 23, 1402
Kim, D.-W., Fabbiano, G., & Trinchieri, G. 1992, ApJ, 393, 134
Kim, D.-W., Fabbiano, G., Mackie, G., & Norman, C. 1994, ApJ, submitted
Kriss, G. A., Cioffi, D. F., & Canizares, C. R. 1983, ApJ, 272, 439
Loewenstein, M. 1989, MNRAS, 283, 15
Lubin, L. M., & Bahcall, N. A. 1993, ApJ, 415, L17
Malin, D. F., & Carter, D. 1983, ApJ, 274, 534
Morrison, R., & McCammon, D. 1983, ApJ, 270, 119
Parma, P., de Ruiter, H. R., Fanti, C., & Fanti, R. 1986, A&AS, 64, 135
Pellegrini, S., & Fabbiano, G. 1994, ApJ, 429, 105
Plucinsky, P. P., Snowden, S. L., Briel, U. G., Hasinger, G., & Pfeferman, E. 1993, ApJ, 418, 519
Ponman, T. J., & Bertram, D. 1993, Nature, 363, 51
Preswitch, A. H., Guimond, S. J., Luginbuhl, C., & Joy, M. 1994, ApJ, accepted
Prugniel, P., Davoust, E., & Nieto, J.-L. 1989, A&A, 222, 5
Raymond, J. C., & Smith, B. W. 1977, ApJS, 35, 419
Sarazin, C. L. 1988, X-Ray Emissions from Clusters of Galaxies (Cambridge: Cambridge Univ. Press)
Sarazin, C. L., & White, R. E. 1987, ApJ, 320, 32
Sarazin, C. L., & Ashe, G. A. 1989, ApJ, 345, 22
Sarazin, C. L., O'Connell, R. W., & McNamara, B. R. 1992a, ApJ, 397, L31
———. 1992b, ApJ, 398, L59
Schweizer, F. 1990, in Dynamics and Chemical Evolution of Elliptical Galaxies, ed. R. Wielen (Heidelberg: Springer), 60
Snowden, S. L., McCammon, D., Burrows, D. N., & Mendenhall, J. A. 1994, ApJ, submitted
Songaila, A., Cowie, L. L., Hogan, C. J., & Rugers, M. 1994, Nature, 368, 599
Stark, A. A., Gammie, C. F., Wilson, R. W., Bally, J., Linke, R. A., Heiles, C., & Hurwitz, M. 1992, ApJS, 79, 77
Tammann, G. A. 1982, in Supernovae: A Survey of Current Research, ed. M. Rees & R. Stoneham (Dordrecht: Reidel), 371
Thomas, P. A., Fabian, A. C., Arnaud, K. A., Forman, W., & Jones, C. 1986, MNRAS, 222, 655
Trinchieri, G., Fabbiano, G., & Canizares, C. R. 1986, ApJ, 310, 637
Trinchieri, G., Kim, D.-W., Fabbiano, G., & Canizares, C. R. 1994, ApJ, 428, 555
van den Bergh, S., & Tammann, G. A. 1991, ARA&A, 29, 363
Vedder, P. W., Trester, J. J., & Canizares, C. R. 1988, ApJ, 332, 275
Walker, T. P., Steigman, G., Schramm, D. N., Olive, K. A., & Kang, H. 1991, ApJ, 376, 51
Wegner, G., Haynes, M. P., & Giovanelli, R. 1993, AJ, 105, 1251
White, D. A., Fabian, A. C., Allen, S. W., Edge, A. C., Crawford, C. S., Johnstone, R. M., Stewart, G. C., & Vogue, W. 1994, MNRAS, 269, 589
White, R. E., & Sarazin, C. L. 1987a, ApJ, 318, 621
———. 1987b, ApJ, 318, 629

© American Astronomical Society • Provided by the NASA Astrophysics Data System